3D electrical conductivity imaging of Halemaʻumaʻu lava lake (Kīlauea volcano)

Lydie Gailler[1*], Jim Kauahikaua[2], Jean-François Lénat[1], André Revil[3], Marceau Gresse[4], Abdellahi Soueid Ahmed [3], Nicolas Cluzel[1], Geeth Manthilake[1], Lucia Gurioli[1], Tim Johnson[5], Anthony Finizola[6], Eric Delcher[6]

[1] Laboratoire Magmas et Volcans, Université Clermont Auvergne, CNRS, IRD, OPGC, Campus Universitaire des Cézeaux, 6 Avenue Blaise Pascal, 63178 AUBIERE Cedex, France

[2] U.S.G.S. Hawaiʻian National Park, PO Box 51, 1 Crater Rim Road, Hawaiʻi National Park, HI 96718

[3] Univ. Grenoble Alpes, Univ. Savoie Mont Blanc, CNRS, IRD, IFSTTAR, ISTerre, 38000 Grenoble, France.

[4] Earthquake Research Institute, University of Tokyo, Tokyo, Japan.

[5] Pacific Northwest National Laboratory, Richland, Washington 99352.

[6] Laboratoire GéoSciences Réunion, Université de la Réunion, IPGP, Sorbonne Paris-Cité, CNRS UMR 7154, 15 Avenue René Cassin, CS 92003, 97744 Saint-Denis, La Réunion, France

Corresponding author: l.gailler@opgc.univ-bpclermont.fr

Abstract

Before the 2018 collapse of the summit of Kīlauea volcano, a ca. 200 m in diameter lava lake inside of Halemaʻumaʻu crater was embedded in a very active hydrothermal system. In 2015, we carried out an electrical conductivity survey and the data were inverted in 3D. The lack of conductivity contrast between the hydrothermal zones and the lava lake precludes to clearly distinguish the lava column. Laboratory measurements on samples from the lava lake show that the conductivity of magma is significantly lower than that of hydrothermal zones but the high vesicularity of the upper part of the lava lake may decrease its macroscopic conductivity. Based on the 3D conductivity model, we distinguish at least two types of hydrothermal circulations: 1) one guided by the collapse faults of Halemaʻumaʻu crater and by the magmatic column of the lava lake, and 2) another guided by previous caldera faults

and fractures related to intrusions. We observe that the location of the faults formed during the 2018 collapse of the summit was greatly influenced by the hydrothermally altered zones.

1- Introduction

The detection of magma at depth and the quantification of its macroscopic properties (melt fraction, volume and magma distribution) are among the most important challenges in volcanology. Geophysical methods such as seismology, deformation, magnetic and electrical resistivity methods may be used for that purpose. Because the velocity and attenuation of elastic waves depend on the mechanic properties of the medium, seismic methods have the potential to detect the presence of magma (Murase and McBirney, 1973). With these methods, the presence of melts has been inferred in various environments from oceanic ridges to the upper mantle of subduction zones and volcanoes (see a review in Lees, 2007). However, the wavelengths of the seismic waves used in these studies are sometimes too large (several tens of kilometers; e.g., Pritchard and Gregg, 2016) to detect small magmatic bodies (a few tens of meters) especially at low depths. In deformation approaches, inflation/deflation cycles of volcanic areas are often interpreted as pressurization/depressurization of magma bodies. Modelling allows estimating the size, depth and geometry of these bodies, but ambiguity remains on the nature of the fluids, because hydrothermal fluids may also generate comparable deformation (e.g., Gambino and Guglielmino, 2008; Hurwitz et al., 2007). Magnetic methods also have a large potential for detecting and imaging magma bodies at depth, because, above the Curie temperature (580°C), the magma is paramagnetic. Thus, in high temperature zones the magnetic signal vanishes. This phenomenon has been used to map the Curie isotherm at great depth at the scale of a large area (e.g. Blakely, 1988; Tanaka et al., 1999: ~5800 x 10^3 km²) or at shallow depth in smaller areas (e.g. Gailler et al., 2016, 2017: ~810 x 10^3 km²). Electrical measurements are well suited for imaging the interior of active volcanoes, because the resistivity of volcanic rocks spans several orders of magnitude (Lénat, 1995) and because magmas have the lowest resistivity values in volcanic environment ranging from about 20 to less than 1 ohm.m (see Lénat et al. 1995 and references therein). However, hydrothermally altered rocks (e.g. zeolites, clay and sulfate minerals) and active hydrothermal systems (hot mineralized fluids, altered rocks) may show resistivity values only slightly larger than that of melts (Legaz et al., 2009; Murase, T., McBirney, 1973; Revil et al., 2008, 2004, 2002; Revil and Jardani, 2010). Studying large magma bodies remains therefore challenging because of the ambiguities in the interpretation of geophysical data for the detection of magma. Active lava lakes are probably the best geological structures where

the capacity of geophysical methods for detecting magma can be ~~carried out~~ tested. There are presently a limited number of active lava lakes: Erta Ale (Ethiopia), Ambrym (Vanuatu), Mount Erebus (Ross Island, Antarctica), Nyiragongo (Democratic Republic of the Congo), Masaya (Nicaragua) and Kīlauea (Hawai‘i) until 2018. Among those, Kīlauea's ~~one~~ was the most ~~suited~~ suitable site to make experiments at close range in terms of accessibility, dimension, depth of the magma column and possibility to collect fresh samples.

In 2015, we carried out an electrical resistivity experiment around Halema‘uma‘u lava lake using multi-electrodes arrays and direct current to probe the lava lake and the extent of its surrounding hydrothermal system. To our knowledge, this is the first time that such measurements were made at close range of a large body of magma. This survey also offers a unique detailed dataset to study the Halema‘uma‘u lava lake before its destruction in May 2018.

2- Geological context

Kīlauea volcano (Hawai‘i) remains undoubtedly an iconic edifice with a complex history of effusive and explosive cycles (Swanson et al., 2014). At least two cycles of explosive and effusive eruptions have occurred in the last 2200 years following collapse of the Powers caldera ca. 200 BCE (Holcomb, 1987; Powers, 1948), and the modern caldera ca. 1500 CE (Swanson et al., 2012). A major feature of the present summit caldera is Halema‘uma‘u crater (Fig. 1). This crater has hosted several lava lakes, with the latest one, informally called Halema‘uma‘u Overlook Crater, first appearing in March 2008 following a small explosive eruption near the SE rim of Halema‘uma‘u crater (Orr et al., 2013). Its surface diameter progressively increased to reach 200 m when it disappeared in 2018 on May 10 during the caldera collapse. A large-scale subsidence of the caldera floor around Halema‘uma‘u began in mid-May and lasted until early August (Neal et al., 2019). The lava lake had been closely monitored by the Hawai‘ian Volcano Observatory (HVO) for hazards reasons and for research. Among the projects aimed at understanding how the lava lake worked and its interactions with Kīlauea's system as a whole, we can underline: seismics (Chouet and Dawson, 2013; Patrick et al., 2011), gravity (Carbone & Poland, 2012; Poland & Carbone, 2016), thermal imaging (Patrick et al., 2015; Patrick et al., 2016), deformation (Richter et al., 2013) as well as quantification and analysis of the products (Eychenne et al., 2015; Swanson et al., 2009).

2.1- The resistivity experiment

Electrical Resistivity Tomography (ERT) field measurements are usually with a quadripole system along profiles: an electrical current is injected into the ground between two current electrodes A and B and the resulting electrical potential distribution is sampled between two voltage electrodes M and N. An apparent resistivity (in ohm.m) can be determined using the electrode geometry, the injected current and the measured difference of electrical potential.

Electrical resistivity measurements were performed in November 2015 around Halemauamau lava lake along ten profiles each 2.5 km in length, using Wenner protocol measurements (more accurate for the detection of horizontal contacts) with a set of 64 stainless steel electrodes with an electrode spacing of 40 meters. A curvilinear geometry of the electrode arrays around the crater (Fig. 1a) was especially tailored to generate current-lines passing through the lava lake along 7 profiles (an example is provided in figure C1 in Supplementary data C). 4945 resistivity measurements were acquired and filtered to remove the low signal-to-noise ratio or spurious data. A 3D ERT (E4D) code from Johnson et al. (2010) was used to derive the conductivity model. A complete description of the parallel inversion algorithm is given in Johnson et al. (2010) (See Supplementary data C for more information).

In order to check the detectability of the conductive magma column, forward theoretical 3D models that depict a conductivity pattern similar to the one expected in the Halema'uma'u area were calculated using E4D software (see figure A1 in Supplementary data A). Three forward models were developed and synthetic data generated from these were inverted to test the effect of 1) a highly conductive lava lake, 2) a large conductive hydrothermal system and 3) the combination of both conductive bodies, all embedded in an overall highly resistive environment (mostly lava flows) as a starting model. Forward modeling was performed to mimic as closely as possible the field conditions ~~and~~ with the same configuration as used for the 3D inversion (mesh, number of elements; see Supplementary data C for additional information). We note that very small structures such as the magma column are difficult to recover even with very low conductive values (i.e. a few S/m). Our forward tests show the primary contribution to the conductivity models is from the hydrothermal system with only a minor affect that could be attributed to the lava lake.

2.2- Microscopic physical properties of the lava lake

Inferring the internal physical state of the lava lake is ~~also~~ fundamental to quantify the in situ conductivity and verify the reliability of the 3D conductivity model. The magma of the lake may be sampled ~~thanks to~~ with ~~bombs~~ ejecta emitted during explosive events and Pele's hair~~s~~ continuously formed by spattering at the surface of the lake. Such samples enable us to carry out laboratory measurements to quantify the electrical conductivity of the magma and the density-derived vesicularity of the pyroclasts.

Electrical conductivity measurements were performed on three Hawai‘ian basaltic glass samples (Fig. C2 in Supplementary data C) using an impedance gain-phase analyzer in the 10^1-10^6 Hz frequency range. The high-pressure and high temperature experiments were performed in a multi-anvil apparatus at Laboratory Magmas et Volcans (LMV). The samples were chosen to represent different degrees of degassing and variable amounts of vesicularity. The low confining pressure (500 MPa) was chosen to preserve the sample vesicles during the initial hydrostatic compression of the high-pressure assembly. The conductivity of basaltic glass increases continuously with increasing temperature from 200 to 1200 °C as shown on figure 2a. Before melting all three samples show similar conductivity values around 10^{-2} S/m. Upon melting, at around 1100 °C, the conductivity of samples discontinuously increased by two orders ~~of~~ by magnitude to ~ 1 S/m at 1200 °C.

For vesicularity measurements, several specimens of lava lake quenched ~~projections~~ ejecta (from 5 to 10 cm in size) produced during explosive events of the Kīlauea lava lake activity, as well as Pele’s hair were sampled. (Fig. C2 in Supplementary data C). Density measurements of the samples were performed using a pycnometer (Micromeritics Geopyc 1360 envelope density analyzer, at Laboratoire Magmas et Volcans-LMV) for samples smaller than 5 cm in diameter. The water immersion technique described in Houghton & Wilson (1989), which is based on Archimedes’ principle, was instead used for samples bigger than 5 cm in diameter. Measurement for both these approaches were determined to a precision of +/- 10^{-2}. The vesicularity was obtained using the dense rock equivalent (DRE) measured with the Accupyc 1340 Helium Pycnometer on the same powdered samples. The same pycnometer was used to measure the connected porosity for each clast using the method described in Formenti and Druitt (2003). We calculated the pore connectivity by dividing the connected porosity by the total porosity. For vesicularity and density measurements, various types of samples were also analysed for petrophysical comparison (Fig. C2 in Supplementary data C).

Our laboratory-based electrical conductivity measurements of Pele's hair~~s~~ and pyroclasts (Fig. 2a) indicate conductivity as high as 1 S/m at temperatures above their melting temperature (~ 1150 °C). The density-derived vesicularity values of the pyroclasts are more than 75 vol. % (Fig. 2b), in agreement with the low density of the upper part of the lava lake suggested by gravity measurements (Carbone et al., 2013; Poland & Carbone, 2016). Because the vesicles of the pyroclasts are totally connected (Fig. 2c), the conductivity values of the melted samples should be representative of that of the lava lake. ~~Indeed, simple~~ Calculations with Sigmelts (Pommier & Le-Trong, 2011) show that for a 1 S/m magma containing 80% of resistive spherical gas vesicles, the bulk conductivity of magma plus vesicles rises to about $1.4\ 10^{-1}$ S/m.

Considering that in a natural system, gas bubbles concentrate in the upper part of the magma column, the conductivity derived from the measurements on the lava lake samples may be considered as a good estimate of that of the upper part of the magma column, as confirmed by the in-situ measurements performed at Kīlauea Iki lava lake (Smith et al, 1977) and lava flow (Bartel et al., 1983). Such low conductivity values are commonly associated with low density materials in agreement with the recent estimated densities of the lava lake (Carbone et al., 2013). Joint analysis of gravity and lava level time series data (Poland & Carbone, 2016) recorded over a large period (2011-2015) have shown a low average density (1000–1500 kg m^{-3}) of the lava within the upper tens to hundreds of meters. As a comparison, density of vesicle-free lava has been estimated in the first ten of meters for other Hawai‘ian lava lakes samples, giving melt fraction density of about 2740 kg m^{-3} for Alae lava lake and 2730 to 2750 kg m^{-3} for Makaopuhi lava lake (Peck, 1978) at temperatures higher than 1100 °C. Accordingly, the very low-density values estimated at the scale of Halema‘uma‘u lava lake can be connected to high vesicularity at least in the upper magma column in the summit vent.

3- Results: 3D conductivity model of a complex volcanic zone

A priori knowledge of the geometry of the magma column ~~of the lava lake~~ would be an important constraint for modelling. It is difficult to establish, but some variations of the lake level have provided insights onto the shape of the magma column at depth. In March 2011, the lake dropped more than 210 m, allowing the mapping of the upper conduit (Orr et al., 2013). The diameter ~~in~~ at the surface was then ~~of~~ 115 m and decreased to about 36 m at 210

m ~~in~~ depth. The vent subsequently widened to the steady surface diameter of nearly 200 m at the time of our survey in 2015 where the top of the magmatic column was varying between the altitude of the floor of Halemaʻumaʻu crater to nearly 200 meters in depth.

3.1- Qualitative observations

The main feature of the 3D model (Fig. 3a and b; Supplementary data B) is that the area of Halemaʻumaʻu is globally conductive. This is in agreement with the strong hydrothermal activity observed at the surface. High conductivity values are particularly extensive all around the crater where surface altered areas are collocated with positive self-potential and temperature anomalies (Fig. 3d). In the southern area of Halemaʻumaʻu crater, two main conductive zones can be distinguished (Fig. 3b and supplementary data B). The one to the southeast (conductor C1 on Figures 3 a and b) coincides in part with the lava lake, and the second, wider one at the southwest, is clearly related to the hydrothermal system (conductor C2 on figure 3 a, b and c). During the collapse of a large part of the caldera, related to the 2018 east rift eruption, we observed that the hydrothermally altered zones coincided with the major faults of the collapse. The superimposition of the 3D conductivity model at 50 m in depth (conductors C3 and C4 on Fig. 3a) or of the extent of the hydrothermal areas (Fig. 3e) with the extent of the collapsed zone between May 31 and July 8 2018, shows this correlation. This consistency is especially well evidenced to the northeast at the scale of the NE conductor C4 (Fig. 3c). At the beginning, the collapse was focused on the area of the lava lake and of the VLP source (Dawson and Chouet, 2014) (Fig 3a). The latter was attributed to the persistent unsteady flow of magma through a complex system of sills and dikes in the shallow plumbing system of Kīlauea (Chouet and Dawson, 2013; Chouet and Matoza, 2013). These observations (*i.e.*, highly conductive zones, seismic activity and collapse focus) demonstrate the connection between the magmatic and hydrothermal systems in this area.

3.2- A magma body concealed in its surrounding hydrothermal system

Based on the conductivity distribution and its values, it is not possible to unambiguously identify the presence of a magma column beneath the lava lake, in agreement with our sensitivity testing from forward modeling using theoretical conductivity patterns (Fig. A1 in Supplementary data A). The presence of wide volumes of hydrothermal alteration and hot fluids implies that the medium has a high general conductivity and therefore a limited conductivity contrast with that expected for the magma column. The 3D conductivity

distribution model and theoretical resistivity estimates allow us to distinguish four main conductivity regions.

1) The area of the lava lake (conductor C1; 1 S/m) coincides with a more diffuse and wider conductive zone than expected for the magmatic body alone.

2) The hydrothermal system surrounding the magmatic column should have slightly lower conductivity values (conductor C1; ~ 1.67 10^{-2} S/m) than the magma column. However, the presence of a large amount of gas bubbles in the upper part of the lake may result in decreasing the conductivity contrast between the magma and the hydrothermal system. Furthermore, the magma column itself is a source of heat and fluids for the surrounding medium. In eight years (since 2008), it is conceivable that a crown of enhanced hydrothermal activity and elevated temperature has developed around the magma column, thus increasing the conductivity in a volume larger than that of the column. Rock alteration by volcanic gases is influenced by the properties of the fumarolic gases (Iwasaki et al., 1964). This pattern is particularly important at Kīlauea where gases emitted near the lava lake are very hot (~600°C) and mostly composed of water and CO_2, but also much of SO_2. We therefore postulate that the high conductivity anomaly in the area of the lava lake is created by a combined effect of both the magma column and by the surrounding hydrothermal amplified system.

3) Away from the magma column of the lava lake, the main conductive areas to the WSW and the patches to the N of Halemaʻumaʻu crater should not be influenced directly by the lava lake, but by deeper sources.

4) The conductive zones lie in a water-unsaturated low temperature medium corresponding to the caldera's dense pile of lava flows (resistant R; > 1500 ohm.m).

3.3- Volcano-tectonic control on the hydrothermal activity

The presence of widespread and strong hydrothermal activity is therefore the main obstacle to clearly differentiate a very high conductivity magma column in this context. The extent of the hydrothermal zones may be refined with the help of the surface thermal anomalies, outcrops of hydrothermal alteration and by the conductivity models.

As it is common in inversion methods, the use of smoothness factors tends to blur the structures at depth and fails to define their depth extent. Accordingly, the conductivity

structures have probably more focused boundaries and vertical extent than are shown in the models. On Figure 3d we have classified the distribution of the hydrothermal system as: (1) highly conductive layer rising to the surface, (2) present at depth or (3) absent. These observations are interpolated with the help of the thermal anomaly map (Patrick & Witzke, 2011) between the profiles. Indeed, it is well established that there is a relationship between surface temperature anomalies and the presence of hydrothermal activity in this context. The sharp and near vertical conductivity contrasts observed on the 2D inversion models of the profiles are also shown on Figure 3d. These characteristics suggest that volcano-tectonic features such as collapse faults and intrusive fractures may control the extent of hydrothermal zones. As shown on figure 3e, the hydrothermally altered zones constitute mechanical heterogeneities and large areas of weakness that influence the development of the collapse faults.

4- Discussion and conclusions

Without the presence of a visible magma column, the interpretation of the resistivity measurements at the summit of Kīlauea would remain ambiguous. Unless the magma body had a huge size or the surrounding medium was resistive, it will always be difficult to distinguish magma in this context. The fact that the upper part of the column is highly vesiculated (as demonstrated by the present study on ejected samples: Fig. 2b, and gravity monitoring by Carbone et al., 2013) may explain why this part of the column has a lower conductivity than that obtained on laboratory measurements considering 80% of resistive spherical gas vesicles.

This high vesicularity further contributes to lowering the conductivity contrast between the hydrothermal zone and the magma column.

Based on the observations at the surface and the interpretation of the modelled conductivity distribution, an interpretative scheme has been constructed (Fig. 4). The east rift eruption of 2018 and the associated summit collapse show that the lava lake was connected to a magma reservoir that was drained during the eruption along the East Rift Zone

Two types of hydrothermal circulation may be present in the studied zone. The first one is associated ~~to~~ with the collapse faults of Halemaʻumaʻu crater. It explains the high conductivity values in Halemaʻumaʻu and on its rim~~s~~. The magmatic column of the lava lake is emplaced along the eastern rim fault of Halemaʻumaʻu crater, which thus acts as preferential pathway for both hydrothermal circulation and magmatic intrusion. For this

reason, the high conductivity values linked to hydrothermal activity and the presence of magma are collocated. This results in the ambiguous identification of the magmatic system within its hydrothermal environment. When the summit vent opened in 2008, one interesting point is that much of the tephra produced in that explosion ~~were~~ was heavily coated with anhydrite and natroalunite. Such samples differ greatly from alteration related to hot springs sinter deposits (Bishop, 2011; DeSmither, 2011), implying that the surficial deposits had been heavily altered by sulfuric acid. Accordingly in the lava lake area, the shallow hydrothermal alteration could be driven from deeper processes. Alteration could therefore be more intense around the magmatic conduit than elsewhere, as suggested by our study.
The second, broader, hydrothermal region is located outside of the crater where elongated hydrothermal zones (with the example of anomaly C3 to the north of the crater, figure 3a and c) are more likely attributed to larger scale fracturing such as ancient caldera rims (Swanson et al., 2012) and/or to dyke-shaped intrusions. These fractures have created weakness or more permeable areas and therefore preferential hydrothermal and magmatic fluids pathways within the edifice.

The model presented in this study is derived from 3D inversion. We show the importance ~~to consider~~ of considering 3D forward models in order to optimize the 3D survey protocol to image the targeted structures. Additional data and more sophisticated 3D electrical modelling software~~s~~ could also depict a clearer picture of such a magmatic body from conductivity data. It remains that our experience has emphasized the difficulties of unambiguously identifying magma at depth with resistivity measurements. This goes beyond the case of Kīlauea, and is an issue in all magmatic systems. In order to address it, more work is necessary in several directions: types of measurements (such as deep 3D ERT, magnetic measurements as an example), laboratory calibration and model computation using complementary datasets. In the case of extensive hydrothermal alteration, the joint study of several geophysical types of data (conductivity, induced polarization, seismic, magnetic) may help to distinguish high conductivity values associated with hydrothermal activity from those associated with magma bodies.

Magmatic bodies and hydrothermally altered rocks are among the main zones of weakness at various depths and lateral extents in volcanoes. The 2018 crisis and the associated major collapse event at Kīlauea volcano is a strong example of the large increase of hazards due to surrounding hydrothermal system. However, the geometry and extent of such systems

remain difficult to constraint in depth. Here we contribute to image the extent of this hydrothermal system both laterally and in depth, that should, at least in part, have an influence on volcano-tectonic evolution. Combining such high-resolution geophysical surveys interpreted under geological and physical constraints therefore remains one of the most powerful tools for quantifying hazards at many other volcanoes (Finn et al., 2001).

REFERENCES

Barde-Cabusson, S., Finizola, A., Revil, A., Ricci, T., Piscitelli, S., Rizzo, E., Angeletti, B., Balasco, M., Bennati, L., Byrdina, S., Carzaniga, N., Crespy, A., Di Gangi, F., Morin, J., Perrone, A., Rossi, M., Roulleau, E., Suski, B., Villeneuve, N., 2009. New geological insights and structural control on fluid circulation in La Fossa cone (Vulcano, Aeolian Islands, Italy). J. Volcanol. Geotherm. Res. 185, 231–245. https://doi.org/10.1016/j.jvolgeores.2009.06.002

Bartel, L. C., Hardee, H. C., Jacobson, R.C., 1983. An electrical resistivity measurement in molten basalt during the 1983 Kilauea eruption. Bull. Volcanol. 46, 271–276.

Bishop, R.A., 2011. Mineralogical study of volcanic sublimates from Halemaʻumaʻu Crater, Kilauea Volcano, Hawaii Space Grant Consortium.

Blakely, R.J., 1988. Curie temperature isotherm analysis and tectonic implications of aeromagnetic data from Nevada. J. Geophys. Res. Solid Earth 93, 11817–11832. https://doi.org/10.1029/JB093iB10p11817

Byrdina, S., Friedel, S., Vandemeulebrouck, J., Budi-Santoso, Suhari, A., Suryanto, W., Rizal, M.H., Winata, Kusdaryanto, E., 2017. Geophysical image of the hydrothermal system of Merapi volcano. , 329, 30-40 (2017). J. Volcanol. Geotherm. Res. 329, 30–40.

Carbone, D., Poland, M.P., 2012. Gravity fluctuations induced by magma convection at Kīlauea volcano, Hawai'i. Geology 40, 803–806. https://doi.org/10.1130/G33060.1

Carbone, D., Poland, M.P., Patrick, M.R., Orr, T.R., 2013. Continuous gravity measurements reveal a low-density lava lake at Kīlauea Volcano, Hawai'i. Earth Planet. Sci. Lett. 376, 178–185. https://doi.org/10.1016/j.epsl.2013.06.024

Chambers, J.E., Kuras, O., Meldrum, P.I., Ogilvy, R.D., Hollands, J., 2006. Electrical resistivity tomography applied to geologic, hydrogeologic, and engineering investigations at a former waste-disposal site. Geophysics 71, B231–B239. https://doi.org/10.1190/1.2360184

Childs, H., Brugger, E., Whitlock, B., Meredith, J., Ahern, S., Pugmire, D., Biagas, K., Miller, M., Harrison, C., Weber, G.H., Krishnan, H., Fogal, T., Sanderson, A., Garth, C., Bethel, E.W., Camp, D., Rubel, O., Durant, M., Favre, J.M., Navratil, P., 2012. High Performance Visualization--Enabling Extreme-Scale Scientific Insight. pp. 357–

372.

Chouet, B., Dawson, P., 2013. Very long period conduit oscillations induced by rockfalls at Kilauea Volcano, Hawaii. J. Geophys. Res. Solid Earth 118, 5352–5371. https://doi.org/10.1002/jgrb.50376

Chouet, B.A., Matoza, R.S., 2013. A multi-decadal view of seismic methods for detecting precursors of magma movement and eruption. J. Volcanol. Geotherm. Res. 252, 108–175. https://doi.org/10.1016/j.jvolgeores.2012.11.013

Dahlin, T., 1996. 2D resistivity surveying for environmental and engineering applications. First Break 14, 275–283.

Dawson, P., Chouet, B., 2014. Characterization of very-long-period seismicity accompanying summit activity at Kīlauea Volcano, Hawai'i: 2007-2013. J. Volcanol. Geotherm. Res. https://doi.org/10.1016/j.jvolgeores.2014.04.010

Dawson, P.B., Benítez, M.C., Chouet, B.A., Wilson, D., Okubo, P.G., 2010. Monitoring very- long- period seismicity at KilaueaVolcano, Hawaii. Geophys. Res. Lett. 37. https://doi.org/10.1029/2010GL044418

DeSmither, L., 2011. Distribution of opaline alteration in fumaroles from Halema'uma'u Crater, Kilauea Volcano., Hawaii Space Grant Consortium.

Eychenne, J., Houghton, B.F., Swanson, D.A., Carey, R.J., Swavely, L., 2015. Dynamics of an open basaltic magma system: The 2008 activity of the Halema'uma'u Overlook vent, Kīlauea Caldera. Earth Planet. Sci. Lett. 409, 49–60. https://doi.org/10.1016/j.epsl.2014.10.045

Finizola, A., Revil, A., Rizzo, E., Piscitelli, S., Ricci, T., Morin, J., Angeletti, B., Mocochain, L., Sortino, F., 2006. Hydrogeological insights at Stromboli volcano (Italy) from geoelectrical, temperature, and CO2 soil degassing investigations. Geophys. Res. Lett. 33, 2–5. https://doi.org/10.1029/2006GL026842

Finizola, A., Ricci, T., Deiana, R., Barde-Cabusson, S., Rossi, M., Praticelli, N., Giocoli, A., Romano, G., Delcher, E., Suski, B., Revil, A., Menny, P., Di Gangi, F., Letort, J., Peltier, A., Villasante-Marcos, V., Douillet, G., Avard, G., Lelli, M., 2010. Adventive hydrothermal circulation on Stromboli volcano (Aeolian Islands, Italy) revealed by geophysical and geochemical approaches: Implications for general fluid flow models on volcanoes. J. Volcanol. Geotherm. Res. 196, 111–119.

https://doi.org/10.1016/j.jvolgeores.2010.07.022.

Finn, C.A., Sisson, T.W., Deszcz-Pan, M., 2001. Aerogeophysical measurements of collapse-prone hydrothermally altered zones at Mount Rainier volcano. Nature 409, 600–603.

Formenti, Y., Druitt, T., 2003. Vesicle connectivity in pyroclasts and implications for the fluidisation of fountain-collapse pyroclastic flows, Montserrat (West Indies). Earth Planet. Sci. Lett. 214. https://doi.org/10.1016/S0012-821X(03)00386-8

Gailler, L.-S., Lénat, J.-F., Blakely, R.J., 2016. Depth to Curie temperature or bottom of the magnetic sources in the volcanic zone of la Réunion hot spot. J. Volcanol. Geotherm. Res. 324. https://doi.org/10.1016/j.jvolgeores.2016.06.005

Gailler, L., Arcay, D., Münch, P., Martelet, G., Thinon, I., Lebrun, J.F., 2017. Forearc structure in the Lesser Antilles inferred from depth to the Curie temperature and thermo-mechanical simulations. Tectonophysics. https://doi.org/10.1016/j.tecto.2017.03.014

Gambino, S., Guglielmino, F., 2008. Ground deformation induced by geothermal processes: A model for La Fossa Crater (Vulcano Island, Italy). J. Geophys. Res. Solid Earth 113, n/a--n/a. https://doi.org/10.1029/2007JB005016

Holcomb, R.T., 1987. Eruptive history and long-term behavior of Kīlauea volcano, in: Volcanism in Hawaii. U.S. Geol. Surv. Prof. Pap. 1350, pp. 261–350.

Houghton, B. F., Wilson, C.J.N., 1989. A vesicularity index for pyroclastic deposits. Bull. Volcanol. 51, 451–462.

Hurwitz, S., Christiansen, L.B., Hsieh, P.A., 2007. Hydrothermal fluid flow and deformation in large calderas: Inferences from numerical simulations. J. Geophys. Res. Solid Earth 112. https://doi.org/10.1029/2006JB004689

Iwasaki, I., Hirayama, M., Katsura, T., Osawa, T., Ossaka, J., Kamada, M., Matsumoto, H., 1964. Alteration of rock by volcanic gas in Japan, in: XIII General Assembly, IUGG.

Johnson, T. C., Versteeg, R. J., Ward, A., Day-Lewis, F. D., Revil, A., 2010. Improved hydrogeophysical characterization and monitoring through high performance electrical geophysical modeling and inversion. Geophysics 75, 27–41.

Johnson, T.C., Versteeg, R.J., Ward, A., Day-Lewis, F.D., Revil, A., 2010. Improved

hydrogeophysical characterization and monitoring through parallel modeling and inversion of time-domain resistivity and induced-polarization data. Geophysics 75, WA27-WA41. https://doi.org/10.1190/1.3475513

Kawabata, E., Cronin, S. J., Bebbington, M.S., Moufti, M.R.H., El-Masry, N., Wang, T., 2015. Identifying Multiple Eruption Phases from a Compound Tephra Blanket: An Example of the AD1256 Al-Madinah Eruption, Saudi Arabia. Bull Volcanol 77.

LaBrecque, D. J., Yang, X., 2001. Difference Inversion of ERT Data: a Fast Inversion Method for 3-D In Situ Monitoring. Soc. Explor. Geophys. 6, 83–89. https://doi.org/https://doi.org/10.4133/JEEG6.2.83

Lees, J.M., 2007. Seismic tomography of magmatic systems. J. Volcanol. Geotherm. Res. 167, 37–56.

Legaz, A., Vandemeulebrouck, J., Revil, A., Kemna, A., Hurst, A.W., Reeves, R., Papasin, R., 2009. A case study of resistivity and self-potential signatures of hydrothermal instabilities, Inferno Crater Lake, Waimangu, New Zealand. Geophys. Res. Lett. 36, L12306. https://doi.org/10.1029/2009GL037573

Lénat, J.F., 1995. Geoelectrical methods in volcano monitoring. in Monitoring Active Volcanoes: Strategies, procedures and techniques., UCL Press London. ed.

Loke, M.H., 2014. 3-D resistivity & IP forward modeling using the finite-difference and finite-element methods.

Murase, T., McBirney, A.R., 1973. Properties of some common igneous rocks and their melts at high temperatures. Geol. Soc. Am. Bull. 84, 5352–5371.

Murase, T., McBirney, A.R., 1973. Properties of some common igneous rocks and their melts at high temperature. Geol. Soc. Am. Bull. 84, 3563– 3592.

Neal, C.A., Brantley, S.R., Antolik, L., Babb, J.L., Burgess, M., Calles, K., Cappos, M., Chang, J.C., Conway, S., Desmither, L., Dotray, P., Elias, T., Fukunaga, P., Fuke, S., Johanson, I.A., Kamibayashi, K., Kauahikaua, J., Lee, R.L., Pekalib, S., Miklius, A., Million, W., Moniz, C.J., Nadeau, A., Okubo, P., Parcheta, C., Patrick, M.R., Shiro, B., Swanson, D.A., Tollett, W., Trusdell, F., Younger, E.F., Zoeller, M.H., Montgomery-Brown, E.K., Anderson, K.R., Poland, M.P., Ball, J.L., Bard, J., Coombs, M., Dietterich, H.R., Kern, C., Thelen, W.A., Cervelli, P.F., Orr, T., Houghton, B.F., Gansecki, C., Hazlett, R., Lundgren, P., Diefenbach, A.K., Lerner, A.H., Waite, G.,

Kelly, P., Clor, L., Werner, C., Mulliken, K., Fisher, G., Damby, D., 2019. The 2018 rift eruption and summit collapse of K ī lauea Volcano. Science (80-.). 363, 367–374.

Neal, C.A., Lockwood, J.P., 2003. Geologic map of the summit region of Kīlauea Volcano, Hawaii: U.S. Geol. Surv. Geol. Investig. Ser. I-2759, scale 124,000, 14 p.

Ni, H., Keppler, H., Behrens, H., 2011. Electrical conductivity of hydrous basaltic melts: Implications for partial melting in the upper mantle. Contrib. to Mineral. Petrol. 162, 637–650. https://doi.org/10.1007/s00410-011-0617-4

Orr, T.R., Thelen, W.A., Patrick, M.R., Swanson, D.A., Wilson, D.C., 2013. Explosive eruptions triggered by rockfalls at Kīlauea volcano, Hawai'i. Geology. https://doi.org/10.1130/G33564.1

Patrick, M. R., and Witzke, C.N., 2011. Thermal mapping of Hawaiian volcanoes with ASTER satellite data. U. S. Geol. Surv. Sci. Investig. Rep. 2011–5110, 22pp.

Patrick, M. R., Orr, T., Lee, L., Moniz, C., 2015. A multipurpose camera system for monitoring Kilauea Volcano, Hawai'I, in: U.S. Geological Survey Techniques and Methods Book 13.

Patrick, M.R., Orr, T., Sutton, A.J., Lev, L., Thelen, W., Fee, D., 2016. Shallowly driven fluctuations in lava lake outgassing (gas pistoning), Kilauea Volcano. Earth Planet. Sci. Lett. 433, 326–338. https://doi.org/10.1016/j.epsl.2015.10.052

Patrick, M., Wilson, D., Fee, D., Orr, T., Swanson, D., 2011. Shallow degassing events as a trigger for very-long-period seismicity at Kīlauea Volcano, Hawai'i. Bull. Volcanol. 73, 1179–1186. https://doi.org/10.1007/s00445-011-0475-y

Peck, D.L., 1978. Cooling and vesiculation of Alae lava lake, Hawaii. U.S. Geol. Surv. Prof. 935B, 59.

Poland, M. P. & Carbone, D., 2016. Insights into shallow magmatic processes at Kīlauea Volcano, Hawai'i, from a multiyear continuous gravity time series. Geophys. Res. Solid Earth 121, 5477–5492.

Pommier, A., Le-Trong, E., 2011. "SIGMELTS": A web portal for electrical conductivity calculations in geosciences. Comput. Geosci. 37, 1450–1459.

Powers, H.A., 1948. A Chronology of the Explosive Eruptions of Kilauea. Pacific Sci. 2, 278–292.

Pritchard, M.E., Gregg, P.M., 2016. Geophysical Evidence for Silicic Crustal Melt in the Continents : Where , What Kind , and How Much ? 121–128. https://doi.org/10.2113/gselements.12.2.121

Revil, A., Finizola, A., Others, and 17, 2008. Inner structure of La Fossa di Vulcano (Vulcano Island, southern Tyrrhenian Sea, Italy) revealed by high resolution electric resistivity tomography coupled with self-potential, temperature, and soil CO2 diffuse degassing measurements. J. Geophys. Res. 113, B07207.

Revil, A., Finizola, A., Sortino, F., Ripepe, M., 2004. Geophysical investigations at Stromboli volcano, Italy: implications for ground water flow and paroxysmal activity. Geophys J Int 157, 426–440.

Revil, A., Hermitte, D., Spangenberg, E., Cochemé, J.J., 2002. Electrical properties of zeolitized volcaniclastic materials. J. Geophys. Res. 107, 2168. https://doi.org/10.1029/2001JB000599

Revil, A., Jardani, A., 2010. Seismoelectric response of heavy oil reservoirs: Theory and numerical modelling. Geophys. J. Int. 180, 781–797. https://doi.org/10.1111/j.1365-246X.2009.04439.x

Richter, N., Poland, M.P., Lundgren, P.R., 2013. TerraSAR-X interferometry reveals small-scale deformation associated with the summit eruption of Kīlauea Volcano, Hawai'i. Geophys. Res. Lett. 40, 1279–1283. https://doi.org/10.1002/grl.50286

Robain, H. & Bobachev, A., 2002. X2IPI : user manual.

Roche, O, Druitt, T. H. & Merle, O., 2000. Experimental study of caldera formation. J. Geophys. Res. 105, 395–416.

Si, H., 2015a. TetGen, a Delaunay-based quality tetrahedral mesh generator. ACM Trans. Math. Softw. 41, 1–36.

Si, H., 2015b. TetGen, a Delaunay-based quality tetrahedral mesh generator. ACM Trans. Math. Softw. 41, 1–36.

Smith, B. D., Zablocki, C. J., Frischknecht, F., Flanigan, V.J., 1977. Summary of results of electromagnetic and galvanic soundings on Kilauea Iki lava lake, Hawaii. US Geol. Surv. Rep. 77–59.

Swanson, D., Wooten, K. & Orr, T., 2009. Buckets of ash track tephra flux from

Halemaʻumaʻu crater, Hawaiʻi. Eos, Trans. Am. Geophys. Union 90, 427.

Swanson, D.A., Rose, T.R., Fiske, R.S., McGeehin, J.P., 2012. Keanakākoʻi Tephra produced by 300 years of explosive eruptions following collapse of Kīlauea Caldera in about 1500 CE. J. Volcanol. Geotherm. Res. 215–216, 8–25. https://doi.org/10.1016/j.jvolgeores.2011.11.009

Swanson, D.A., Rose, T.R., Mucek, A.E., Garcia, M.O., Fiske, R.S., Mastin, L.G., 2014. Cycles of explosive and effusive eruptions at Kīlauea Volcano, Hawaiʻi. Geology2 42, 631–634. https://doi.org/10.1130/G35701.1 (IP-055751)

Tanaka, A., Okubo, Y., Matsubayashi, O., 1999. Curie point depth based on spectrum analysis of the magnetic anomaly data in East and Southeast Asia. Tectonophysics 306, 461–470. https://doi.org/http://dx.doi.org/10.1016/S0040-1951(99)00072-4

Zablocki, C.J., 1976. Mapping thermal anomalies on an active volcano by the selfpotential method, Kilauea, Hawaii. Proceedings, 2nd U.N. Symp. Dev. use Geotherm. Resour. San Fr. California, May 1975 2, 1299–1309.

Acknowledgements This study was funded by the Laboratory of Excellence ClerVolc and partly on behalf of a CNRS INSU project. We are grateful to Tina Neal, Jeff Sutton, Don Swanson, Steve Brantley and all the HVO's staff, Philippe Labazuy, Thierry Souriot, Yohan Gardes and the OPGC staff, for their scientific and logistic support, before, during and after the survey. We also thank the Hawai'i Volcanoes National Park for their support, and USGS as information sources. We also warmly acknowledge all the volunteers, Bernadette Lénat, Bernard Contarin, Béatrice Chevallet and Guy Chevallet, for their contribution to this project. Thanks for the technical advices of STRATAGEM974 for the preparation of the ERT field work and data processing. This is Laboratory of Excellence ClerVolc contribution n° XX. Computations presented in this paper were performed using the Froggy platform of the CIMENT infrastructure (https://ciment.ujf-grenoble. fr), which is supported by the Rhône-Alpes region (grant CPER07_13 CIRA), the OSUG@2020 labex (reference ANR10 LABX56), and the Equip@Meso project (reference ANR-10-EQPX-29-01) of the program 'Investissements d'Avenir' supervised by the Agence Nationale pour la Recherche. 3D conductivity images were generated thanks to VisIt software. The manuscript greatly benefited from the comments and reviews from Alessandro Aiuppa, Donald Swanson an anonymous reviewer, to whom we offer our thanks.

Figure captions

In main text

Figure 1: **The Lava lake of Kīlauea Volcano.** a) Location of the ERT profiles around the lava lake in Halema'uma'u crater in the summit caldera of Kīlauea Volcano; base map is a lidar image with 1 m resolution. Location of the active lava lake is shown. b) weak spattering that produces Pele's hair, Pele's tears, and other glassy pyroclasts. c) Explosive event triggered by a rock fall into the lava lake and producing highly vesicular spatter. d) Gas plume during typical lava lake activity. Photos obtained from https://volcanoes.usgs.gov/volcanoes/Kīlauea/archive/multimedia/index.shtml.

Figure 2: **Measurements on lava lake samples: a)** Evolution of the conductivity measurements with temperature for each sample : glassy and vesicular parts of pyroclasts shown as assemblages before the experiment, Pele's hair crushed before melting. The blue shaded area indicates electrical resisitivity of hydrous basalt at high temperature (Ni et al, 2011) b) Comparison of the vesicularity (%) of the lava lake ejecta with several types of samples in the environment of the crater. c) Diagram of bulk vesiculatity versus connected vesicularity showing that all the bubbles are connected.

Figure 3: 3D conductivity model of the lava lake and its environment a) at a depth of 50 m below the lava lake surface. RMS 6, 18 iterations. DEM from http://opentopo.sdsc.edu/lidarDataset?opentopoID=OTLAS.032012.32605.1. The radar image (Italian Space Agency's Cosmo-SkyMed satellite system;

https://volcanoes.usgs.gov/observatories/hvo/multimedia_uploads/multimediaFile-2556.gif) in right-bottom inset shows enlargement of summit eruptive vent from May 31 and July 8, 2018. The black star locates the VLP source from Dawson et al. (2010). b) SWRZ-lava lake-ERZ slice within the 3D model shown in a, and associated sensitivity. A zoom on the lava lake is framed in red. c) NW-SE and SW-NE slices within the 3D model shown in a. Areas unconstrained in the model are blanked (i.e. sensitivity <-10). 3D topography from Google Earth. d) Qualitative comparison between 3D and 2D models showing the main distribution of the hydrothermal system superimposed to the thermal anomaly map. Main eruptive axis from (Neal and Lockwood, 2003). e) 2018 crisis main axes of fracturing and subsidence of Halema'uma'u crater and caldera floor on July 8, 2018 (georeferenced from radar images and WorldView-3 satellite; USGS-HVO website) superimposed to the distribution of the hydrothermal system inferred from conductivity model and thermal anomaly map.

Figure 4: **Synthetic interpretative scheme**, derived from our 3D conductivity model combined with geological information such as fracturing (Roche et al., 2000) and zones of alteration based on thermal anomaly map (Patrick & Witzke, 2011).

In Supplementary data A

Figure A1: Inversion of synthetic models using E4D software. a) Theoretical models and recovered conductivity distribution after inversion. b) Horizontal slices within 3D inversions.

In Supplementary data B

Movie of the 3D inversion. The video file was generated by VisIT software (Childs et al., 2012).

In Supplementary data C

Figure C1: **Example of 2D conductivity model for a profile crossing the lava lake** (located on the left). SP measurements acquired during this survey and temperature from thermal anomaly map (Patrick, M. R., and Witzke, 2011) are shown for comparison.

Figure C2: Location and photo of the analyzed samples.

Supplementary data A

Theoretical conductivity signal of the lava lake investigated through 3D direct modeling

As explained in the main text, the presence of widespread hydrothermal alteration in Halema'uma'uarea creates large zones of high conductivity values that make it difficult to extract the signal of the conductive magma column. The detectability of the conductive magma column may be checked on theoretical models that depict a conductivity pattern similar to the one that is expected in the Halema'uma'u area. We have thus built synthetic models and computed their response using E4D software (Johnson et al., 2010). The forward models simulates the direct current potential field for the survey. Then, this set of synthetic data is inverted. Forward modelling and inversion were executed on the same mesh built with the TetGen algorithm (Si, 2015). It consists of 465 electrode locations, 240,275 finite-element nodes, and 1,397,631 tetrahedral elements 6000 m^3 in volume and a maximum cell size of 18 m by side (see Supplementary data C for additional information). To simulate field data, forward modelling was conducted considering the same number of measurements and the same electrode distribution than those of the original survey (Fig. 1 in the main text). Five per cent of normally distributed noise was added to each of the final 3859 measurements and a transfer resistance magnitude of $M = 0.1$ (i.e. 10% error) was defined to be consistent with the initial 3D inversion. The synthetic data were inverted using the same option and convergence criteria as did the 3D conductivity model. Tests were made for three conceptual models shown in Fig. A1. We consider an overall highly resistive environment (mostly lava flows) typical of a basaltic system as a starting model (~10 000 Ω.m; 10^{-4} S/m).

1- Model A: the effect of a small vertical conductive conduit to simulate the lava lake (conductivity of ~1 S/m according to our petrophysical measurements on samples) in its resistive surrounding (10^{-4} S/m).
2- Model B: The effect of a large hydrothermal system (conductivity of ~2.10^{-2} S/m are common values observed in similar volcanic systems (*e.g.* (Byrdina et al., 2017; Finizola et al., 2010; Revil and Jardani, 2010)) in the same resistive surrounding). Note that the extent of this conductive structure has been limited to the Halema'uma'ucrater.
3- Model C: The combination of both conductive bodies (*i.e.* the lava lake within the hydrothermal system) within the initial resistive model. In order to deteremine the minimum conductivity difference for the magma body to be imaged within the hydrothermal system, we have also tested several conductivity values for the hydrothermal system (Model C1: ~2.10^{-2}, Model C2: ~10^{-2}, Model C3: ~5.10^{-3} S/m).

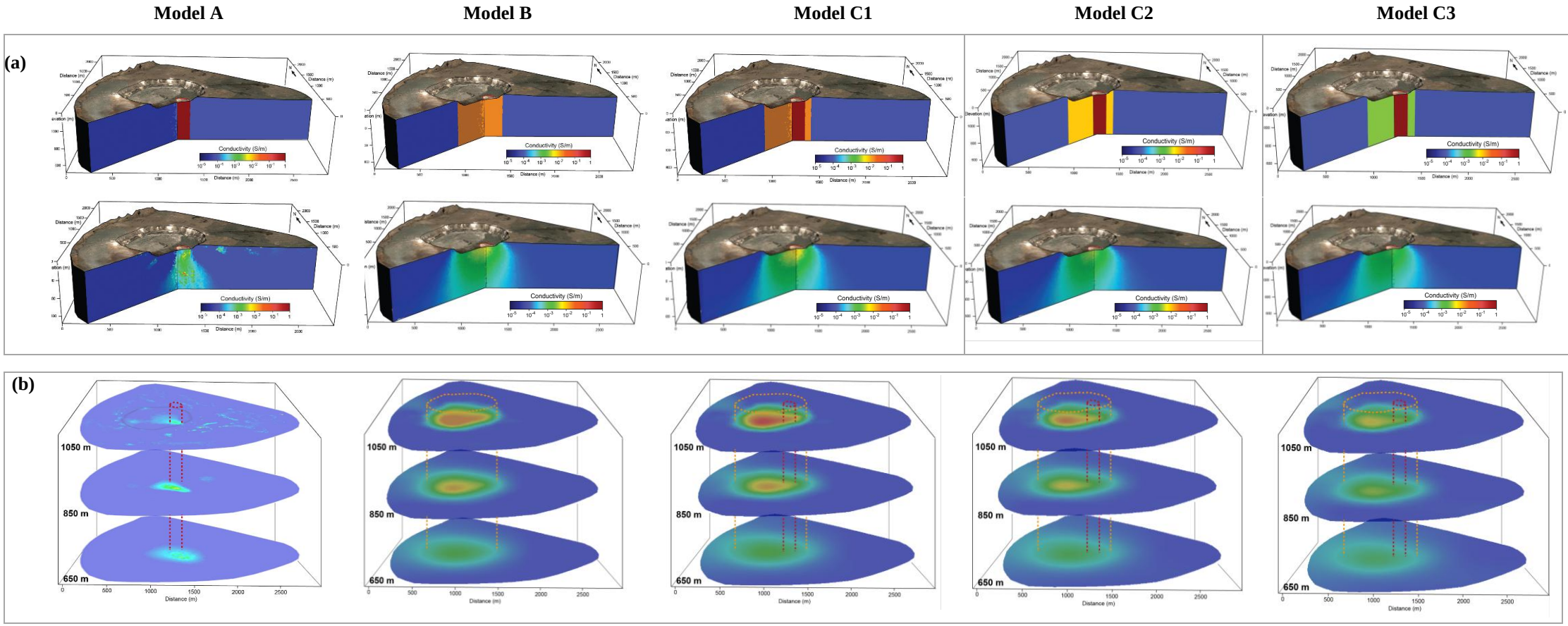


Figure A1: Inversion of synthetic models using E4D software. a) Theoretical models and recovered conductivity distribution after inversion. b) Horizontal slices within 3D inversions.

In the case of a single highly conductive column that simulates the lava lake alone (Model A), the initial very high conductivity value (1 S/m) is not recovered with the inversion. A more diffuse and lower conductive structure is observed with values ranging between 1.10^{-2} - $2\ 10^{-2}$ S/m. This latter is clearly less resolved in depth, and no more detectable at a depth of 200-300 m below the surface, as evidenced on the NW-SE slice (Fig. A1 Model A).
For a single hydrothermal system (Fig. A1 Model B), conductive values are well recovered in the central part of the crater. Laterally and more in depth, the geometry of the resulting conductive structure departs from the initial synthetic model. This is attributable to the low current line density at depth, with the electrode configuration employed.

~~The~~ Model C integrates both the magmatic column and the hydrothermal system with three different conductivity contrasts (Model C1, C2 and C3 in Fig. A1). Being more consistent with the actual geology (*i.e.* a lava lake embedded in a large hydrothermal system within a resistive pile of lava flows), this last model is therefore closer to the conductivity distribution obtained for our survey.As for the hydrothermal system case, the geometry of the resulting conductive structure departs from the initial synthetic model especially in depth for the same reasons as above. We note that model C1 ($\sim 2.10^{-2}$ S/m) gives results very close to model B, with, after all, a slightly higher conductivity structure in the area of the magma column from the surface to a depth of about 850 m (Fig. A1 b). Nevertheless, this feature progressively disappears while increasing the conductivity contrast between the magma body and the hydrothermal system (Models C2 and C3 in Fig. A1).

With these tests, we can better assess the ~~sensibility~~ sensitivity of our field measurements and, consequently their limitation for the lava lake detection. The measurements of our survey have limits for resolving contrasts at depth and lateral contacts. The high conductivity hydrothermal system dominates the results and blurs the signature of the magma column. However, the conductive lava lake has a slight, but perceptible effect within a very high conductive hydrothermal system (i.e. lower than 2.10^{-2} S/m).

References

Barde-Cabusson, S., Finizola, A., Revil, A., Ricci, T., Piscitelli, S., Rizzo, E., Angeletti, B., Balasco, M., Bennati, L., Byrdina, S., Carzaniga, N., Crespy, A., Di Gangi, F., Morin, J., Perrone, A., Rossi, M., Roulleau, E., Suski, B., Villeneuve, N., 2009. New geological insights and structural control on fluid circulation in La Fossa cone (Vulcano, Aeolian Islands, Italy). J. Volcanol. Geotherm. Res. 185, 231–245.

https://doi.org/10.1016/j.jvolgeores.2009.06.002

Bartel, L. C., Hardee, H. C., Jacobson, R.C., 1983. An electrical resistivity measurement in molten basalt during the 1983 Kilauea eruption. Bull. Volcanol. 46, 271–276.

Bishop, R.A., 2011. Mineralogical study of volcanic sublimates from Halemaʻumaʻu Crater, Kilauea Volcano, Hawaii Space Grant Consortium.

Blakely, R.J., 1988. Curie temperature isotherm analysis and tectonic implications of aeromagnetic data from Nevada. J. Geophys. Res. Solid Earth 93, 11817–11832. https://doi.org/10.1029/JB093iB10p11817

Byrdina, S., Friedel, S., Vandemeulebrouck, J., Budi-Santoso, Suhari, A., Suryanto, W., Rizal, M.H., Winata, Kusdaryanto, E., 2017. Geophysical image of the hydrothermal system of Merapi volcano. , 329, 30-40 (2017). J. Volcanol. Geotherm. Res. 329, 30–40.

Carbone, D., Poland, M.P., 2012. Gravity fluctuations induced by magma convection at Kīlauea volcano, Hawai'i. Geology 40, 803–806. https://doi.org/10.1130/G33060.1

Carbone, D., Poland, M.P., Patrick, M.R., Orr, T.R., 2013. Continuous gravity measurements reveal a low-density lava lake at Kīlauea Volcano, Hawai'i. Earth Planet. Sci. Lett. 376, 178–185. https://doi.org/10.1016/j.epsl.2013.06.024

Chambers, J.E., Kuras, O., Meldrum, P.I., Ogilvy, R.D., Hollands, J., 2006. Electrical resistivity tomography applied to geologic, hydrogeologic, and engineering investigations at a former waste-disposal site. Geophysics 71, B231–B239. https://doi.org/10.1190/1.2360184

Childs, H., Brugger, E., Whitlock, B., Meredith, J., Ahern, S., Pugmire, D., Biagas, K., Miller, M., Harrison, C., Weber, G.H., Krishnan, H., Fogal, T., Sanderson, A., Garth, C., Bethel, E.W., Camp, D., Rubel, O., Durant, M., Favre, J.M., Navratil, P., 2012. High Performance Visualization--Enabling Extreme-Scale Scientific Insight. pp. 357–372.

Chouet, B., Dawson, P., 2013. Very long period conduit oscillations induced by rockfalls at Kilauea Volcano, Hawaii. J. Geophys. Res. Solid Earth 118, 5352–5371. https://doi.org/10.1002/jgrb.50376

Chouet, B.A., Matoza, R.S., 2013. A multi-decadal view of seismic methods for detecting precursors of magma movement and eruption. J. Volcanol. Geotherm. Res. 252, 108–175. https://doi.org/10.1016/j.jvolgeores.2012.11.013

Dahlin, T., 1996. 2D resistivity surveying for environmental and engineering applications. First Break 14, 275–283.

Dawson, P., Chouet, B., 2014. Characterization of very-long-period seismicity accompanying summit activity at Kīlauea Volcano, Hawai'i: 2007-2013. J. Volcanol. Geotherm. Res. https://doi.org/10.1016/j.jvolgeores.2014.04.010

Dawson, P.B., Benítez, M.C., Chouet, B.A., Wilson, D., Okubo, P.G., 2010. Monitoring very- long- period seismicity at KilaueaVolcano, Hawaii. Geophys. Res. Lett. 37. https://doi.org/10.1029/2010GL044418

DeSmither, L., 2011. Distribution of opaline alteration in fumaroles from Halema'uma'u Crater, Kilauea Volcano., Hawaii Space Grant Consortium.

Eychenne, J., Houghton, B.F., Swanson, D.A., Carey, R.J., Swavely, L., 2015. Dynamics of an open basaltic magma system: The 2008 activity of the Halema'uma'u Overlook vent, Kīlauea Caldera. Earth Planet. Sci. Lett. 409, 49–60. https://doi.org/10.1016/j.epsl.2014.10.045

Finizola, A., Revil, A., Rizzo, E., Piscitelli, S., Ricci, T., Morin, J., Angeletti, B., Mocochain, L., Sortino, F., 2006. Hydrogeological insights at Stromboli volcano (Italy) from geoelectrical, temperature, and CO2 soil degassing investigations. Geophys. Res. Lett. 33, 2–5. https://doi.org/10.1029/2006GL026842

Finizola, A., Ricci, T., Deiana, R., Barde-Cabusson, S., Rossi, M., Praticelli, N., Giocoli, A., Romano, G., Delcher, E., Suski, B., Revil, A., Menny, P., Di Gangi, F., Letort, J., Peltier, A., Villasante-Marcos, V., Douillet, G., Avard, G., Lelli, M., 2010. Adventive hydrothermal circulation on Stromboli volcano (Aeolian Islands, Italy) revealed by geophysical and geochemical approaches: Implications for general fluid flow models on volcanoes. J. Volcanol. Geotherm. Res. 196, 111–119. https://doi.org/10.1016/j.jvolgeores.2010.07.022.

Finn, C.A., Sisson, T.W., Deszcz-Pan, M., 2001. Aerogeophysical measurements of collapse-prone hydrothermally altered zones at Mount Rainier volcano. Nature 409,

600–603.

Formenti, Y., Druitt, T., 2003. Vesicle connectivity in pyroclasts and implications for the fluidisation of fountain-collapse pyroclastic flows, Montserrat (West Indies). Earth Planet. Sci. Lett. 214. https://doi.org/10.1016/S0012-821X(03)00386-8

Gailler, L.-S., Lénat, J.-F., Blakely, R.J., 2016. Depth to Curie temperature or bottom of the magnetic sources in the volcanic zone of la Réunion hot spot. J. Volcanol. Geotherm. Res. 324. https://doi.org/10.1016/j.jvolgeores.2016.06.005

Gailler, L., Arcay, D., Münch, P., Martelet, G., Thinon, I., Lebrun, J.F., 2017. Forearc structure in the Lesser Antilles inferred from depth to the Curie temperature and thermo-mechanical simulations. Tectonophysics. https://doi.org/10.1016/j.tecto.2017.03.014

Gambino, S., Guglielmino, F., 2008. Ground deformation induced by geothermal processes: A model for La Fossa Crater (Vulcano Island, Italy). J. Geophys. Res. Solid Earth 113, n/a--n/a. https://doi.org/10.1029/2007JB005016

Holcomb, R.T., 1987. Eruptive history and long-term behavior of Kīlauea volcano, in: Volcanism in Hawaii. U.S. Geol. Surv. Prof. Pap. 1350, pp. 261–350.

Houghton, B. F., Wilson, C.J.N., 1989. A vesicularity index for pyroclastic deposits. Bull. Volcanol. 51, 451–462.

Hurwitz, S., Christiansen, L.B., Hsieh, P.A., 2007. Hydrothermal fluid flow and deformation in large calderas: Inferences from numerical simulations. J. Geophys. Res. Solid Earth 112. https://doi.org/10.1029/2006JB004689

Iwasaki, I., Hirayama, M., Katsura, T., Osawa, T., Ossaka, J., Kamada, M., Matsumoto, H., 1964. Alteration of rock by volcanic gas in Japan, in: XIII General Assembly, IUGG.

Johnson, T. C., Versteeg, R. J., Ward, A., Day-Lewis, F. D., Revil, A., 2010. Improved hydrogeophysical characterization and monitoring through high performance electrical geophysical modeling and inversion. Geophysics 75, 27–41.

Johnson, T.C., Versteeg, R.J., Ward, A., Day-Lewis, F.D., Revil, A., 2010. Improved hydrogeophysical characterization and monitoring through parallel modeling and inversion of time-domain resistivity and induced-polarization data. Geophysics 75,

WA27-WA41. https://doi.org/10.1190/1.3475513

Kawabata, E., Cronin, S. J., Bebbington, M.S., Moufti, M.R.H., El-Masry, N., Wang, T., 2015. Identifying Multiple Eruption Phases from a Compound Tephra Blanket: An Example of the AD1256 Al-Madinah Eruption, Saudi Arabia. Bull Volcanol 77.

LaBrecque, D. J., Yang, X., 2001. Difference Inversion of ERT Data: a Fast Inversion Method for 3-D In Situ Monitoring. Soc. Explor. Geophys. 6, 83–89. https://doi.org/https://doi.org/10.4133/JEEG6.2.83

Lees, J.M., 2007. Seismic tomography of magmatic systems. J. Volcanol. Geotherm. Res. 167, 37–56.

Legaz, A., Vandemeulebrouck, J., Revil, A., Kemna, A., Hurst, A.W., Reeves, R., Papasin, R., 2009. A case study of resistivity and self-potential signatures of hydrothermal instabilities, Inferno Crater Lake, Waimangu, New Zealand. Geophys. Res. Lett. 36, L12306. https://doi.org/10.1029/2009GL037573

Lénat, J.F., 1995. Geoelectrical methods in volcano monitoring. in Monitoring Active Volcanoes: Strategies, procedures and techniques., UCL Press London. ed.

Loke, M.H., 2014. 3-D resistivity & IP forward modeling using the finite-difference and finite-element methods.

Murase, T., McBirney, A.R., 1973. Properties of some common igneous rocks and their melts at high temperatures. Geol. Soc. Am. Bull. 84, 5352–5371.

Murase, T., McBirney, A.R., 1973. Properties of some common igneous rocks and their melts at high temperature. Geol. Soc. Am. Bull. 84, 3563– 3592.

Neal, C.A., Brantley, S.R., Antolik, L., Babb, J.L., Burgess, M., Calles, K., Cappos, M., Chang, J.C., Conway, S., Desmither, L., Dotray, P., Elias, T., Fukunaga, P., Fuke, S., Johanson, I.A., Kamibayashi, K., Kauahikaua, J., Lee, R.L., Pekalib, S., Miklius, A., Million, W., Moniz, C.J., Nadeau, A., Okubo, P., Parcheta, C., Patrick, M.R., Shiro, B., Swanson, D.A., Tollett, W., Trusdell, F., Younger, E.F., Zoeller, M.H., Montgomery-Brown, E.K., Anderson, K.R., Poland, M.P., Ball, J.L., Bard, J., Coombs, M., Dietterich, H.R., Kern, C., Thelen, W.A., Cervelli, P.F., Orr, T., Houghton, B.F., Gansecki, C., Hazlett, R., Lundgren, P., Diefenbach, A.K., Lerner, A.H., Waite, G.,

Kelly, P., Clor, L., Werner, C., Mulliken, K., Fisher, G., Damby, D., 2019. The 2018 rift eruption and summit collapse of K ī lauea Volcano. Science (80-.). 363, 367–374.

Neal, C.A., Lockwood, J.P., 2003. Geologic map of the summit region of Kīlauea Volcano, Hawaii: U.S. Geol. Surv. Geol. Investig. Ser. I-2759, scale 124,000, 14 p.

Ni, H., Keppler, H., Behrens, H., 2011. Electrical conductivity of hydrous basaltic melts: Implications for partial melting in the upper mantle. Contrib. to Mineral. Petrol. 162, 637–650. https://doi.org/10.1007/s00410-011-0617-4

Orr, T.R., Thelen, W.A., Patrick, M.R., Swanson, D.A., Wilson, D.C., 2013. Explosive eruptions triggered by rockfalls at Kīlauea volcano, Hawai'i. Geology. https://doi.org/10.1130/G33564.1

Patrick, M. R., and Witzke, C.N., 2011. Thermal mapping of Hawaiian volcanoes with ASTER satellite data. U. S. Geol. Surv. Sci. Investig. Rep. 2011–5110, 22pp.

Patrick, M. R., Orr, T., Lee, L., Moniz, C., 2015. A multipurpose camera system for monitoring Kilauea Volcano, Hawai'I, in: U.S. Geological Survey Techniques and Methods Book 13.

Patrick, M.R., Orr, T., Sutton, A.J., Lev, L., Thelen, W., Fee, D., 2016. Shallowly driven fluctuations in lava lake outgassing (gas pistoning), Kilauea Volcano. Earth Planet. Sci. Lett. 433, 326–338. https://doi.org/10.1016/j.epsl.2015.10.052

Patrick, M., Wilson, D., Fee, D., Orr, T., Swanson, D., 2011. Shallow degassing events as a trigger for very-long-period seismicity at Kīlauea Volcano, Hawai'i. Bull. Volcanol. 73, 1179–1186. https://doi.org/10.1007/s00445-011-0475-y

Peck, D.L., 1978. Cooling and vesiculation of Alae lava lake, Hawaii. U.S. Geol. Surv. Prof. 935B, 59.

Poland, M. P. & Carbone, D., 2016. Insights into shallow magmatic processes at Kīlauea Volcano, Hawai'i, from a multiyear continuous gravity time series. Geophys. Res. Solid Earth 121, 5477–5492.

Pommier, A., Le-Trong, E., 2011. "SIGMELTS": A web portal for electrical conductivity calculations in geosciences. Comput. Geosci. 37, 1450–1459.

Powers, H.A., 1948. A Chronology of the Explosive Eruptions of Kilauea. Pacific Sci. 2, 278–292.

Pritchard, M.E., Gregg, P.M., 2016. Geophysical Evidence for Silicic Crustal Melt in the Continents : Where , What Kind , and How Much ? 121–128. https://doi.org/10.2113/gselements.12.2.121

Revil, A., Finizola, A., Others, and 17, 2008. Inner structure of La Fossa di Vulcano (Vulcano Island, southern Tyrrhenian Sea, Italy) revealed by high resolution electric resistivity tomography coupled with self-potential, temperature, and soil CO2 diffuse degassing measurements. J. Geophys. Res. 113, B07207.

Revil, A., Finizola, A., Sortino, F., Ripepe, M., 2004. Geophysical investigations at Stromboli volcano, Italy: implications for ground water flow and paroxysmal activity. Geophys J Int 157, 426–440.

Revil, A., Hermitte, D., Spangenberg, E., Cochemé, J.J., 2002. Electrical properties of zeolitized volcaniclastic materials. J. Geophys. Res. 107, 2168. https://doi.org/10.1029/2001JB000599

Revil, A., Jardani, A., 2010. Seismoelectric response of heavy oil reservoirs: Theory and numerical modelling. Geophys. J. Int. 180, 781–797. https://doi.org/10.1111/j.1365-246X.2009.04439.x

Richter, N., Poland, M.P., Lundgren, P.R., 2013. TerraSAR-X interferometry reveals small-scale deformation associated with the summit eruption of Kīlauea Volcano, Hawai'i. Geophys. Res. Lett. 40, 1279–1283. https://doi.org/10.1002/grl.50286

Robain, H. & Bobachev, A., 2002. X2IPI : user manual.

Roche, O, Druitt, T. H. & Merle, O., 2000. Experimental study of caldera formation. J. Geophys. Res. 105, 395–416.

Si, H., 2015a. TetGen, a Delaunay-based quality tetrahedral mesh generator. ACM Trans. Math. Softw. 41, 1–36.

Si, H., 2015b. TetGen, a Delaunay-based quality tetrahedral mesh generator. ACM Trans. Math. Softw. 41, 1–36.

Smith, B. D., Zablocki, C. J., Frischknecht, F., Flanigan, V.J., 1977. Summary of results of electromagnetic and galvanic soundings on Kilauea Iki lava lake, Hawaii. US Geol. Surv. Rep. 77–59.

Swanson, D., Wooten, K. & Orr, T., 2009. Buckets of ash track tephra flux from Halemaʻumaʻu crater, Hawaiʻi. Eos, Trans. Am. Geophys. Union 90, 427.

Swanson, D.A., Rose, T.R., Fiske, R.S., McGeehin, J.P., 2012. Keanakākoʻi Tephra produced by 300 years of explosive eruptions following collapse of Kīlauea Caldera in about 1500 CE. J. Volcanol. Geotherm. Res. 215–216, 8–25. https://doi.org/10.1016/j.jvolgeores.2011.11.009

Swanson, D.A., Rose, T.R., Mucek, A.E., Garcia, M.O., Fiske, R.S., Mastin, L.G., 2014. Cycles of explosive and effusive eruptions at Kīlauea Volcano, Hawaiʻi. Geology2 42, 631–634. https://doi.org/10.1130/G35701.1 (IP-055751)

Tanaka, A., Okubo, Y., Matsubayashi, O., 1999. Curie point depth based on spectrum analysis of the magnetic anomaly data in East and Southeast Asia. Tectonophysics 306, 461–470. https://doi.org/http://dx.doi.org/10.1016/S0040-1951(99)00072-4

Zablocki, C.J., 1976. Mapping thermal anomalies on an active volcano by the selfpotential method, Kilauea, Hawaii. Proceedings, 2nd U.N. Symp. Dev. use Geotherm. Resour. San Fr. California, May 1975 2, 1299–1309.

Supplementary data C

Details on ERT and physical measurements

1- Electrical Resistivity Tomography (ERT): principle and inversion

We have used the Electrical Resistivity Tomography (ERT) method, initially developed for environmental investigations and engineering (Chambers et al., 2006; Dahlin, 1996; Loke, 2014). Because a large range of resistivity values is expected in volcanic fields, this imaging technique is therefore now widely used in volcanology (Barde-Cabusson et al., 2009; Finizola et al., 2006; Revil et al., 2008). Knowing the electrical resistivity structures of the subsurface can be very appealing for imaging and monitoring active volcanoes and their hydrothermal systems because the resistivity is sensitive to a number of parameters including, porosity, water content, alteration, salinity, and temperature which play a major role in the characterization of hydrothermal systems (Legaz et al., 2009; Revil et al., 2004, 2002; Revil and Jardani, 2010). Resistivity measurements were performed in November 2015 along ten profiles each 2.5 km in length, using a set of 64 brass electrodes with a take-out of 40 meters. A total of 4945 apparent resistivity measurements were acquired all around the lava lake, using particular geometry of profiles. The data acquisition was performed using a multi-electrode ABEM system (Terrameter SAS 4000) associated with an electrode selector (ES10-64). The study area is characterized by massive lava flows whose surface required drilling in order to connect the electrodes to the ground along each profile. Each measurement is obtained as the mean of 2 to 4 distinct measurements stacked together with the same set of AB (current)-MN (potential) electrodes. Even if contact between the electrodes and the ground was improved by adding salty water and clay at each electrode location, it remained difficult to inject more than 1 mA in the ground, because of the highly resistive nature of the shallow formations. Apparent resistivity values are derived from array measurements with a good signal to-noise ratio. SP measurements have been also performed along each line (an example of 2D conductivity profile is provided in figure C1).

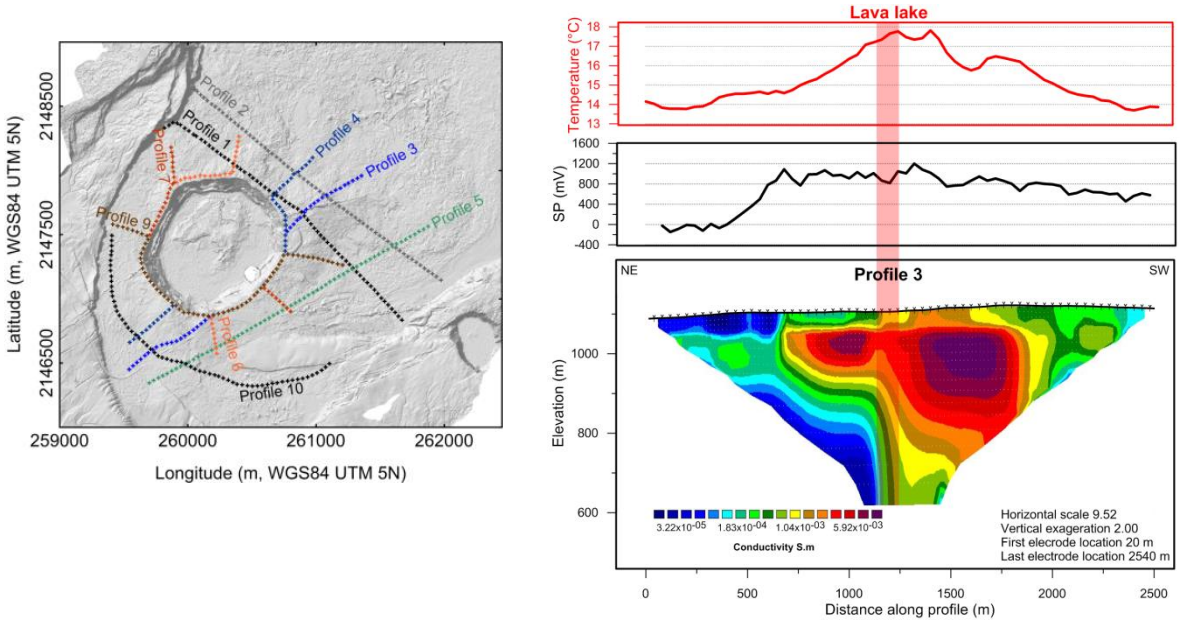


Figure C1: Example of 2D conductivity model for a profile crossing the lava lake (located on the left). SP measurements acquired during this survey and temperature from thermal anomaly map (Patrick and Witzke, 2011) are shown for comparison.

The reliability of final conductivity distribution models largely depends on the quality of the data. To avoid at least a part of data noise, the continuity of the cable and its insulation were tested before the acquisition in the field where the contact electrodes-ground was improved by the addition of salty water and clays sampled directly on site.

Every apparent conductivity corresponds to the mean value of several measurements (stacking). Based on their standard deviation, a data error is estimated from the standard deviation of these measurements and is used for further data filtering. On the one hand, a manual filter was applied in order to remove the low signal to noise ratio of the data. Excluding criteria are a measured electrical potential difference inferior to 1 mV and a standard deviation superior to 5% of the value. The remaining random noise can be taken into account during data inversion. A second filter was applied using X2IPI software (Robain & Bobachev, 2002). Indeed, the presence of strong heterogeneities in the shallow highly resistive levels generates artifacts in the measured signal, which are responsible for inclined anomalies named “C-effect”, in the case of a Wenner array, and hide smoother effects linked to large and deep objects. They were removed in order to recover clearer 2D responses linked to deep and large heterogeneities. A total of 3859 filtered data was then used to build the 3D model.

It was expected that the use of a curvilinear geometry of the profiles would produce a tomogram of the lava lake plumbing system in 3D inversion. To compute the electrical potential associated with a given conductivity distribution, ones need to use a forward operator. In the ERT method, this is given by the Poisson equation which can be solved using a numerical approach such as the finite elements method. We first computed the pole solution for each electrode used as a current source or sink. The potential distribution for a dipole AB source/sink current pair is then constructed by subtracting the pole potential associated with the current sink. We implemented a true 3D inversion approach in a parallel environment using 144 processors on the CIMENT infrastructure (see acknowledgement). A complete description of the parallel inversion algorithm can be found in (Johnson et al., 2010).

To gauge the convergence of the inverse problem, we use an objective function, which is the sum of two terms: the data misfit and the model constraints (model regularizer). In other words, this reflects the fact that we are looking to a solution, which while reproducing the observed data with high fidelity, reflects as well the spatial heterogeneities and structures of the subsurface.

The regularization operator is formulated so that the regularization error increases as the estimated conductivity structure deviates from homogeneity. The objective function is minimized with the Gauss-Newton algorithm as described by (Johnson et al., 2010). To construct the mesh, known topography was used over the survey area and extrapolated further away to avoid edge effects.

The 3-D unstructured mesh of the Hawai‘i crater was built using the TetGen algorithm (Si, 2015). The computational mesh consists of 465 electrode locations, 240,275 finite-element nodes, and 1,397,631 tetrahedral elements 6000 m^3 in volume and a maximum cell size of 18 m by side. The relatively large number of elements with respect to the number of data in this case was required to 1) accurately model the complicated surface topography with a 10-m resolution DEM, and 2) obtain a spatial discretization higher than inter electrode spacing. This enabled us to well constrain the 3D inversion geometry close to the lake (at least in its eastern part) and along the conductivity profiles.

The inversion converges when the normalized χ^2 statistic (i.e. the squared RMS) reaches 1 if the data are appropriately weighted according to equation (1):

$$\chi^2 = \frac{1}{N}\sum_{i=1}^{N}\left(\frac{d_{pred,i}-d_{obs,i}}{\sigma_i}\right)^2, \quad (1)$$

where N is the total number of transfer resistance data and σ_i is the standard deviation of the transfer resistance given by the following criteria proposed by (LaBrecque & Yang, 2001) following equation (2):

$$\sigma_i = M\, d_{obs,i} + \gamma, \quad (2)$$

Even if forward modelling errors are typically no more than 5% of transfer resistance magnitude, we use M = 0.1 (i.e. 10% error) for all data to take into account the data noise. In addition, filtered data standard deviations are often lower than forwarding modelling errors, such that forward modeling errors determine the appropriate convergence criteria. Accordingly, the data may be slightly under-fit when χ^2 =1, but not over-fit, and therefore free from over-fitting induced artifacts.

γ = 0.001 Ω is considered as the instrument precision, and prevents measurements with excessively small transfer resistance magnitudes from dominating the inversion.

Despite the lack of measurements inside Halema‘uma‘u crater, the sensitivity map (Figure 3c) shows that the resolution remains acceptable along and between the measurement profiles at depth down to about 200-300 m. However, model resolution at a particular scale is not a function of the number of elements in the model. It is a function of the information provided by the data. The inverse computations were conducted on 9 nodes (1 master and 8 slave nodes), requiring approximately 12 hours (17 Gauss-Newton iterations) for convergence. Convergence criteria are generally set based upon data error. That is, when the L2 norm of the data misfit reduces to a value that is consistent with the estimated data noise, the inverse solution is assumed to have converged.

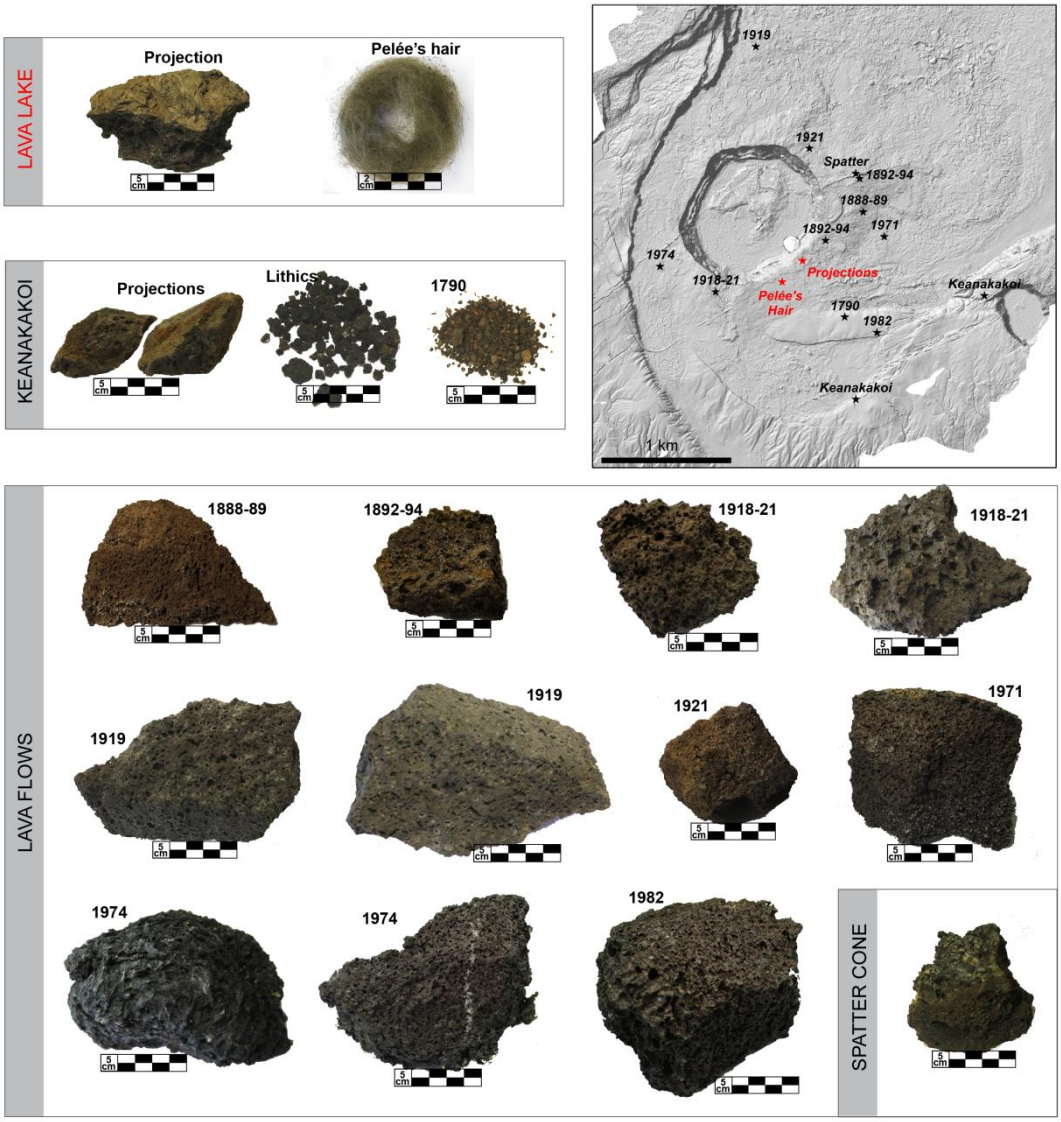


Figure C2: Location and photo of the analyzed samples.

1- Physical measurements

Analyzed samples are shown in figure C2. Several specimens of lava lake, quenched projections (from 5 to 10 cm in size) as well as Pele's hair, were sampled in the environment of the magmatic column. Additionally, 11 samples of lava flows and 1 sample of spatter cone ranging in size from 5 to 15 cm, 3 samples of pyroclasts from the last explosive period ~~event~~ (Keanakāko'i), ranging in size from 0.5 to 5 cm were collected for physical comparison. The strategy of field sampling was designed to sample most of the main formations (type and ages) outcropping at the scale of the caldera.

2-a Electrical conductivity measurements

The electrical conductivity measurements were performed in 25/17 assembly, with a 25 mm edge length Cr_2O_3-doped MgO octahedral pressure medium and 17 mm WC anvil

truncation. A stepped graphite heater was used in order to reduce the axial temperature gradient. Temperatures during the experiments were monitored using a $W_{97}Re_3$–$W_{75}Re_{25}$ thermocouple (D type). The uncertainty on temperature measurements is expected to be less than ±10 °C.

Electrical conductivity was determined using the impedance spectroscopy method in the frequency range of 10^6 -10^1 Hz. Insulation resistance (detection limit) of the assembly at similar pressure-temperature conditions was determined prior to the actual experiments, which was several orders of magnitude lower than the sample resistance. We have also applied corrections for the resistance of the electrode wires. Before melting of glass, the sample resistance was measured in several heating-cooling cycles at temperature steps of 50-100 K until the heating and cooling paths were reproducible. This minimizes the uncertainty of electrical conductivity measurements.

Polycrystalline samples are characterized by a combination of resistor-capacitor / constant phase element (R-C/CPE) circuits and the resistance can be obtained by fitting the impedance spectra to appropriate equivalent circuits. Once the sample resistance has been determined, conductivity can be calculated using the sample diameter and length measured before and after each experiment, assuming the sample geometry remained unchanged during the experiment. The uncertainties in the estimation of the electrical conductivity results from the estimations of temperature, sample dimensions and data fitting errors and are less than 5 %.

2-b Vesicularity measurements

Prior to performing density measurements, samples were dried in an oven at a temperature of 70 °C for 24 h. For the water immersion technique (Houghton & Wilson, 1989), the dry samples were weighed in air (ω_{air} in g), and then wrapped in parafilm squares. Each square is weighed (0.04 g/square) and the number of squares used to wrap the sample counted (nb_{film}). This makes the sample waterproof before immersion in water, thus avoiding water infiltration into the rock. The sample is then weighed once more, after immersion in water (ω_{water} in g). The two weights, plus the number of parafilm squares used, are then used to obtain the rock density (ρ_{BULK} in g/cm^3) from:

$$\rho_{BULCK} = \frac{\omega_{air}}{\omega_{air} - \omega_{water} + \left(0.04\ x\ nb_{film}\right)}$$

Vesicularity ($\emptyset_b$) can be calculated from the dense rock density (ρ_{DRE} in g/cm3) and the rock bulk density (ρ_{BULCK} in g/cm3).

$$\emptyset_b = 100\left(1 - \frac{\rho_{BULK}}{\rho_{DRE}}\right).$$

The bulk density of samples smaller than 5 cm in diameter were performed using a pycnometer (Micromeritics Geopyc 1360 envelope density analyzer, at LMV). As already presented by (Kawabata et al., 2015), the Geopyc instrument can measure the envelope density of objects of different sizes and shapes. Envelope density is the mass of an object divided by its volume, where the volume includes that of its pores and small cavities. The measurement technique uses a quasi-fluid composed of small, rigid spheres (< 1 mm in diameter) having a high degree of fluidity; this medium is called DryFlo™. The sample is placed in a bed of DryFlo and the DryFlo is agitated and gently consolidated around the sample. The envelope volume of a sample is determined by the difference in how far the plunger is driven (by a stepping motor) into a cylinder containing only DryFlo and then when sample is added. The steps of the motor (C) are counted and used to calculate volume. The counts are converted to volume by multiplying them by the conversion factor (v, cm^3/count). The conversion factor is displayed as cm^3/mm. The default envelope volume of the sample V is then the difference in the counts with the sample present $C_{present}$ and with it absent C_{absent} multiplied by v:

$$V = [(C_{present} - C_{absent})v]cm^3$$

When a calibration test is made with a sample of known volume V, the above equation is solved for v. This value of v then becomes the conversion factor (conversion factors expressed as cm^3/mm are similarly derived). The envelope density of the sample is its mass W divided by its envelope volume V.

The connectivity measurements were obtained using an AccuPyc II 1340 Gas Displacement Helium Pycnometer available at LMV. This instrument performs measurement of the skeletal volume of powders and solids that fill sample chambers of 10-100-350 cm^3. This is well adapted for vesicularity measurements because the helium can enter even the smallest vesicles. The total volume of the sample (solids+vesicles; V_{sam}) is obtained from the two methods previously described. Measurement with the pycnometer gives the volume V_{meas} of the solid phases (glass+crystals) plus the volume of any isolated vesicles. The connected

vesicularity (X_c) is given by:

$$X_c = 1 - \frac{V_{meas}}{V_{sam}}$$

The same samples are then crushed (grain size of about 20-30 µm) and the volume again determined using the pycnometer. This then gives the mean density of the solid phases in each sample (ρ_s). The total vesicularity (X_t) is then given by:

$$X_t = 1 - \frac{m_{mas}}{\rho_s V_{sam}}$$

where m_{sam} is the mass of the sample. The fraction of isolated vesicle is given by $X_t - X_c$.

REFERENCES

Barde-Cabusson, S., Finizola, A., Revil, A., Ricci, T., Piscitelli, S., Rizzo, E., Angeletti, B., Balasco, M., Bennati, L., Byrdina, S., Carzaniga, N., Crespy, A., Di Gangi, F., Morin, J., Perrone, A., Rossi, M., Roulleau, E., Suski, B., Villeneuve, N., 2009. New geological insights and structural control on fluid circulation in La Fossa cone (Vulcano, Aeolian Islands, Italy). J. Volcanol. Geotherm. Res. 185, 231–245. https://doi.org/10.1016/j.jvolgeores.2009.06.002

Bartel, L. C., Hardee, H. C., Jacobson, R.C., 1983. An electrical resistivity measurement in molten basalt during the 1983 Kilauea eruption. Bull. Volcanol. 46, 271–276.

Bishop, R.A., 2011. Mineralogical study of volcanic sublimates from Halema‘uma‘u Crater, Kilauea Volcano, Hawaii Space Grant Consortium.

Blakely, R.J., 1988. Curie temperature isotherm analysis and tectonic implications of aeromagnetic data from Nevada. J. Geophys. Res. Solid Earth 93, 11817–11832. https://doi.org/10.1029/JB093iB10p11817

Byrdina, S., Friedel, S., Vandemeulebrouck, J., Budi-Santoso, Suhari, A., Suryanto, W., Rizal, M.H., Winata, Kusdaryanto, E., 2017. Geophysical image of the hydrothermal system of Merapi volcano. , 329, 30-40 (2017). J. Volcanol. Geotherm. Res. 329, 30–40.

Carbone, D., Poland, M.P., 2012. Gravity fluctuations induced by magma convection at Kīlauea volcano, Hawai’i. Geology 40, 803–806. https://doi.org/10.1130/G33060.1

Carbone, D., Poland, M.P., Patrick, M.R., Orr, T.R., 2013. Continuous gravity measurements reveal a low-density lava lake at Kīlauea Volcano, Hawai'i. Earth Planet. Sci. Lett. 376, 178–185. https://doi.org/10.1016/j.epsl.2013.06.024

Chambers, J.E., Kuras, O., Meldrum, P.I., Ogilvy, R.D., Hollands, J., 2006. Electrical resistivity tomography applied to geologic, hydrogeologic, and engineering investigations at a former waste-disposal site. Geophysics 71, B231–B239. https://doi.org/10.1190/1.2360184

Childs, H., Brugger, E., Whitlock, B., Meredith, J., Ahern, S., Pugmire, D., Biagas, K., Miller, M., Harrison, C., Weber, G.H., Krishnan, H., Fogal, T., Sanderson, A., Garth, C., Bethel, E.W., Camp, D., Rubel, O., Durant, M., Favre, J.M., Navratil, P., 2012. High Performance Visualization--Enabling Extreme-Scale Scientific Insight. pp. 357–372.

Chouet, B., Dawson, P., 2013. Very long period conduit oscillations induced by rockfalls at Kilauea Volcano, Hawaii. J. Geophys. Res. Solid Earth 118, 5352–5371. https://doi.org/10.1002/jgrb.50376

Chouet, B.A., Matoza, R.S., 2013. A multi-decadal view of seismic methods for detecting precursors of magma movement and eruption. J. Volcanol. Geotherm. Res. 252, 108–175. https://doi.org/10.1016/j.jvolgeores.2012.11.013

Dahlin, T., 1996. 2D resistivity surveying for environmental and engineering applications. First Break 14, 275–283.

Dawson, P., Chouet, B., 2014. Characterization of very-long-period seismicity accompanying summit activity at Kīlauea Volcano, Hawai'i: 2007-2013. J. Volcanol. Geotherm. Res. https://doi.org/10.1016/j.jvolgeores.2014.04.010

Dawson, P.B., Benítez, M.C., Chouet, B.A., Wilson, D., Okubo, P.G., 2010. Monitoring very- long- period seismicity at KilaueaVolcano, Hawaii. Geophys. Res. Lett. 37. https://doi.org/10.1029/2010GL044418

DeSmither, L., 2011. Distribution of opaline alteration in fumaroles from Halema'uma'u Crater, Kilauea Volcano., Hawaii Space Grant Consortium.

Eychenne, J., Houghton, B.F., Swanson, D.A., Carey, R.J., Swavely, L., 2015. Dynamics of

an open basaltic magma system: The 2008 activity of the Halema'uma'u Overlook vent, Kīlauea Caldera. Earth Planet. Sci. Lett. 409, 49–60. https://doi.org/10.1016/j.epsl.2014.10.045

Finizola, A., Revil, A., Rizzo, E., Piscitelli, S., Ricci, T., Morin, J., Angeletti, B., Mocochain, L., Sortino, F., 2006. Hydrogeological insights at Stromboli volcano (Italy) from geoelectrical, temperature, and CO2 soil degassing investigations. Geophys. Res. Lett. 33, 2–5. https://doi.org/10.1029/2006GL026842

Finizola, A., Ricci, T., Deiana, R., Barde-Cabusson, S., Rossi, M., Praticelli, N., Giocoli, A., Romano, G., Delcher, E., Suski, B., Revil, A., Menny, P., Di Gangi, F., Letort, J., Peltier, A., Villasante-Marcos, V., Douillet, G., Avard, G., Lelli, M., 2010. Adventive hydrothermal circulation on Stromboli volcano (Aeolian Islands, Italy) revealed by geophysical and geochemical approaches: Implications for general fluid flow models on volcanoes. J. Volcanol. Geotherm. Res. 196, 111–119. https://doi.org/10.1016/j.jvolgeores.2010.07.022.

Finn, C.A., Sisson, T.W., Deszcz-Pan, M., 2001. Aerogeophysical measurements of collapse-prone hydrothermally altered zones at Mount Rainier volcano. Nature 409, 600–603.

Formenti, Y., Druitt, T., 2003. Vesicle connectivity in pyroclasts and implications for the fluidisation of fountain-collapse pyroclastic flows, Montserrat (West Indies). Earth Planet. Sci. Lett. 214. https://doi.org/10.1016/S0012-821X(03)00386-8

Gailler, L.-S., Lénat, J.-F., Blakely, R.J., 2016. Depth to Curie temperature or bottom of the magnetic sources in the volcanic zone of la Réunion hot spot. J. Volcanol. Geotherm. Res. 324. https://doi.org/10.1016/j.jvolgeores.2016.06.005

Gailler, L., Arcay, D., Münch, P., Martelet, G., Thinon, I., Lebrun, J.F., 2017. Forearc structure in the Lesser Antilles inferred from depth to the Curie temperature and thermo-mechanical simulations. Tectonophysics. https://doi.org/10.1016/j.tecto.2017.03.014

Gambino, S., Guglielmino, F., 2008. Ground deformation induced by geothermal processes: A model for La Fossa Crater (Vulcano Island, Italy). J. Geophys. Res. Solid Earth 113, n/a--n/a. https://doi.org/10.1029/2007JB005016

Holcomb, R.T., 1987. Eruptive history and long-term behavior of Kīlauea volcano, in: Volcanism in Hawaii. U.S. Geol. Surv. Prof. Pap. 1350, pp. 261–350.

Houghton, B. F., Wilson, C.J.N., 1989. A vesicularity index for pyroclastic deposits. Bull. Volcanol. 51, 451–462.

Hurwitz, S., Christiansen, L.B., Hsieh, P.A., 2007. Hydrothermal fluid flow and deformation in large calderas: Inferences from numerical simulations. J. Geophys. Res. Solid Earth 112. https://doi.org/10.1029/2006JB004689

Iwasaki, I., Hirayama, M., Katsura, T., Osawa, T., Ossaka, J., Kamada, M., Matsumoto, H., 1964. Alteration of rock by volcanic gas in Japan, in: XIII General Assembly, IUGG.

Johnson, T. C., Versteeg, R. J., Ward, A., Day-Lewis, F. D., Revil, A., 2010. Improved hydrogeophysical characterization and monitoring through high performance electrical geophysical modeling and inversion. Geophysics 75, 27–41.

Johnson, T.C., Versteeg, R.J., Ward, A., Day-Lewis, F.D., Revil, A., 2010. Improved hydrogeophysical characterization and monitoring through parallel modeling and inversion of time-domain resistivity and induced-polarization data. Geophysics 75, WA27-WA41. https://doi.org/10.1190/1.3475513

Kawabata, E., Cronin, S. J., Bebbington, M.S., Moufti, M.R.H., El-Masry, N., Wang, T., 2015. Identifying Multiple Eruption Phases from a Compound Tephra Blanket: An Example of the AD1256 Al-Madinah Eruption, Saudi Arabia. Bull Volcanol 77.

LaBrecque, D. J., Yang, X., 2001. Difference Inversion of ERT Data: a Fast Inversion Method for 3-D In Situ Monitoring. Soc. Explor. Geophys. 6, 83–89. https://doi.org/https://doi.org/10.4133/JEEG6.2.83

Lees, J.M., 2007. Seismic tomography of magmatic systems. J. Volcanol. Geotherm. Res. 167, 37–56.

Legaz, A., Vandemeulebrouck, J., Revil, A., Kemna, A., Hurst, A.W., Reeves, R., Papasin, R., 2009. A case study of resistivity and self-potential signatures of hydrothermal instabilities, Inferno Crater Lake, Waimangu, New Zealand. Geophys. Res. Lett. 36, L12306. https://doi.org/10.1029/2009GL037573

Lénat, J.F., 1995. Geoelectrical methods in volcano monitoring. in Monitoring Active

Volcanoes: Strategies, procedures and techniques., UCL Press London. ed.

Loke, M.H., 2014. 3-D resistivity & IP forward modeling using the finite-difference and finite-element methods.

Murase, T., McBirney, A.R., 1973. Properties of some common igneous rocks and their melts at high temperatures. Geol. Soc. Am. Bull. 84, 5352–5371.

Murase, T., McBirney, A.R., 1973. Properties of some common igneous rocks and their melts at high temperature. Geol. Soc. Am. Bull. 84, 3563– 3592.

Neal, C.A., Brantley, S.R., Antolik, L., Babb, J.L., Burgess, M., Calles, K., Cappos, M., Chang, J.C., Conway, S., Desmither, L., Dotray, P., Elias, T., Fukunaga, P., Fuke, S., Johanson, I.A., Kamibayashi, K., Kauahikaua, J., Lee, R.L., Pekalib, S., Miklius, A., Million, W., Moniz, C.J., Nadeau, A., Okubo, P., Parcheta, C., Patrick, M.R., Shiro, B., Swanson, D.A., Tollett, W., Trusdell, F., Younger, E.F., Zoeller, M.H., Montgomery-Brown, E.K., Anderson, K.R., Poland, M.P., Ball, J.L., Bard, J., Coombs, M., Dietterich, H.R., Kern, C., Thelen, W.A., Cervelli, P.F., Orr, T., Houghton, B.F., Gansecki, C., Hazlett, R., Lundgren, P., Diefenbach, A.K., Lerner, A.H., Waite, G., Kelly, P., Clor, L., Werner, C., Mulliken, K., Fisher, G., Damby, D., 2019. The 2018 rift eruption and summit collapse of K ī lauea Volcano. Science (80-.). 363, 367–374.

Neal, C.A., Lockwood, J.P., 2003. Geologic map of the summit region of Kīlauea Volcano, Hawaii: U.S. Geol. Surv. Geol. Investig. Ser. I-2759, scale 124,000, 14 p.

Ni, H., Keppler, H., Behrens, H., 2011. Electrical conductivity of hydrous basaltic melts: Implications for partial melting in the upper mantle. Contrib. to Mineral. Petrol. 162, 637–650. https://doi.org/10.1007/s00410-011-0617-4

Orr, T.R., Thelen, W.A., Patrick, M.R., Swanson, D.A., Wilson, D.C., 2013. Explosive eruptions triggered by rockfalls at Kīlauea volcano, Hawai'i. Geology. https://doi.org/10.1130/G33564.1

Patrick, M. R., and Witzke, C.N., 2011. Thermal mapping of Hawaiian volcanoes with ASTER satellite data. U. S. Geol. Surv. Sci. Investig. Rep. 2011–5110, 22pp.

Patrick, M. R., Orr, T., Lee, L., Moniz, C., 2015. A multipurpose camera system for monitoring Kilauea Volcano, Hawai'I, in: U.S. Geological Survey Techniques and

Methods Book 13.

Patrick, M.R., Orr, T., Sutton, A.J., Lev, L., Thelen, W., Fee, D., 2016. Shallowly driven fluctuations in lava lake outgassing (gas pistoning), Kilauea Volcano. Earth Planet. Sci. Lett. 433, 326–338. https://doi.org/10.1016/j.epsl.2015.10.052

Patrick, M., Wilson, D., Fee, D., Orr, T., Swanson, D., 2011. Shallow degassing events as a trigger for very-long-period seismicity at Kīlauea Volcano, Hawai'i. Bull. Volcanol. 73, 1179–1186. https://doi.org/10.1007/s00445-011-0475-y

Peck, D.L., 1978. Cooling and vesiculation of Alae lava lake, Hawaii. U.S. Geol. Surv. Prof. 935B, 59.

Poland, M. P. & Carbone, D., 2016. Insights into shallow magmatic processes at Kīlauea Volcano, Hawai'i, from a multiyear continuous gravity time series. Geophys. Res. Solid Earth 121, 5477–5492.

Pommier, A., Le-Trong, E., 2011. "SIGMELTS": A web portal for electrical conductivity calculations in geosciences. Comput. Geosci. 37, 1450–1459.

Powers, H.A., 1948. A Chronology of the Explosive Eruptions of Kilauea. Pacific Sci. 2, 278–292.

Pritchard, M.E., Gregg, P.M., 2016. Geophysical Evidence for Silicic Crustal Melt in the Continents : Where , What Kind , and How Much ? 121–128. https://doi.org/10.2113/gselements.12.2.121

Revil, A., Finizola, A., Others, and 17, 2008. Inner structure of La Fossa di Vulcano (Vulcano Island, southern Tyrrhenian Sea, Italy) revealed by high resolution electric resistivity tomography coupled with self-potential, temperature, and soil CO2 diffuse degassing measurements. J. Geophys. Res. 113, B07207.

Revil, A., Finizola, A., Sortino, F., Ripepe, M., 2004. Geophysical investigations at Stromboli volcano, Italy: implications for ground water flow and paroxysmal activity. Geophys J Int 157, 426–440.

Revil, A., Hermitte, D., Spangenberg, E., Cochemé, J.J., 2002. Electrical properties of zeolitized volcaniclastic materials. J. Geophys. Res. 107, 2168. https://doi.org/10.1029/2001JB000599

Revil, A., Jardani, A., 2010. Seismoelectric response of heavy oil reservoirs: Theory and numerical modelling. Geophys. J. Int. 180, 781–797. https://doi.org/10.1111/j.1365-246X.2009.04439.x

Richter, N., Poland, M.P., Lundgren, P.R., 2013. TerraSAR-X interferometry reveals small-scale deformation associated with the summit eruption of Kīlauea Volcano, Hawai'i. Geophys. Res. Lett. 40, 1279–1283. https://doi.org/10.1002/grl.50286

Robain, H. & Bobachev, A., 2002. X2IPI : user manual.

Roche, O, Druitt, T. H. & Merle, O., 2000. Experimental study of caldera formation. J. Geophys. Res. 105, 395–416.

Si, H., 2015a. TetGen, a Delaunay-based quality tetrahedral mesh generator. ACM Trans. Math. Softw. 41, 1–36.

Si, H., 2015b. TetGen, a Delaunay-based quality tetrahedral mesh generator. ACM Trans. Math. Softw. 41, 1–36.

Smith, B. D., Zablocki, C. J., Frischknecht, F., Flanigan, V.J., 1977. Summary of results of electromagnetic and galvanic soundings on Kilauea Iki lava lake, Hawaii. US Geol. Surv. Rep. 77–59.

Swanson, D., Wooten, K. & Orr, T., 2009. Buckets of ash track tephra flux from Halema'uma'u crater, Hawai'i. Eos, Trans. Am. Geophys. Union 90, 427.

Swanson, D.A., Rose, T.R., Fiske, R.S., McGeehin, J.P., 2012. Keanakāko'i Tephra produced by 300 years of explosive eruptions following collapse of Kīlauea Caldera in about 1500 CE. J. Volcanol. Geotherm. Res. 215–216, 8–25. https://doi.org/10.1016/j.jvolgeores.2011.11.009

Swanson, D.A., Rose, T.R., Mucek, A.E., Garcia, M.O., Fiske, R.S., Mastin, L.G., 2014. Cycles of explosive and effusive eruptions at Kīlauea Volcano, Hawai'i. Geology2 42, 631–634. https://doi.org/10.1130/G35701.1 (IP-055751)

Tanaka, A., Okubo, Y., Matsubayashi, O., 1999. Curie point depth based on spectrum analysis of the magnetic anomaly data in East and Southeast Asia. Tectonophysics 306, 461–470. https://doi.org/http://dx.doi.org/10.1016/S0040-1951(99)00072-4